Chapter 4
Characteristics of Biased Electrode Discharges in HSX

4.0 Introduction

To facilitate an understanding of the viscous damping measurements, it is necessary to describe the general properties of the HSX plasma response to the electrode bias. When the electrode voltage is applied, there are changes in the plasma electric field, plasma rotation, plasma turbulence, and plasma wall interactions. This chapter provides the experimental details of these phenomena.

Section 4.1 provides a brief general description of the structure of the experiments. Section 4.2 details the current and voltage relationships of the electrode. The dependence of the electrode current on electrode voltage and electrode location is described. Section 4.3 illustrates the changes in the macroscopic plasma parameters during the electrode voltage pulse. Details of the evolution of the plasma density, H_α emission, and radiated power are provided. Section 4.4 contains details of the plasma flow and electric field response to the electrode bias. Profiles of the floating potential and plasma flow are provided, for times both before and during electrode bias. The time evolution of the spin-up and spin-down are described in detail. Data analysis techniques are provided which allow the extraction of time scales and flow directions from the measured flow and floating potential evolution. These data analysis techniques are applied to discharges with and without symmetry in Section 4.5, illustrating the measured increase in damping when the quasi-symmetry is broken. Section 4.6 describes some of the simple turbulence characteristics of these biased plasmas.

4.1 Explanation of the Experiments

The general structure of the experiments is shown in figure 4.1. The electrode is inserted inside the separatrix to typically r/a ≈0.6-0.7. It is biased positively with respect to the vessel wall via the biased electrode power supply, drawing electrons off the surface on which it resides. These electrons are drawn through the electrode, through the power supply to the vessel, and then back through the plasma to the electrode to complete the circuit. It is assumed that this "return current" flowing through the plasma from the wall to the electrode is poloidally and toroidally uniform. The return current causes a **j**×**B** torque on the plasma, which induces plasma rotation. In steady state, the amount of current drawn is such that the **j**×**B** force balances the forces damping the plasma flow. Hence, the current drawn is directly related to the mechanisms which damp the flows.

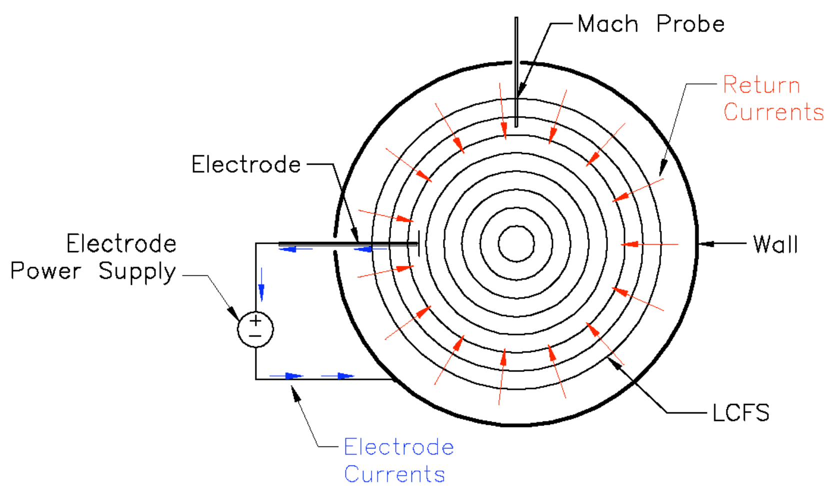

Figure 4.1: The conceptual layout of the experiments.

To measure the rotation of the plasma induced by the return current, the Mach probes described in Section 2.2 are used. They are typically inserted into the region of the plasma between the separatrix and the surface where the biased electrode resides. Hence, these probes are able to measure the plasma flows in the region through which the return current is flowing. It is possible to compile profiles of the measured quantities on a shot by shot basis,.

The subsequent sections in this chapter will discuss the experimental measurements pertaining to this picture. Later chapters will concentrate on the theoretical relationship between the plasma parameters, the magnetic geometry, the radial current, and the bias induced flows.

4.2 The Voltage/Current Characteristics of the Biased Electrode.

The first step in understanding the characteristics of electrode biased discharges is to study the waveform of the electrode, shown in figure 4.2. The ECH is turned on at t=.800, and turned off at t=0.850. The power supply is pulsed up to six times during the discharge. When the electrode is energized, the voltage rises very quickly ($\approx 1\mu s$) to a steady value, while the current has an initial spike before settling down to a steady value. At electrode bias turn-off, the electrode current is broken by the IGBT switches. The electrode current stops very quickly (1-2 μs), while the electrode voltage decays on a longer time scale of typically ~$40\mu s$. Note that there is some modulation of the density during the voltage pulse. The width of the bias pulse was kept small (1.5 msec.) to avoid excessive modulation of the density. Both the voltage on the capacitor bank and the voltage on the electrode are shown; the difference is due to the voltage dropped across the series internal resistance of the power supply. Each of the points mentioned in this paragraph will be visited in more detail below.

The I-V characteristics of the electrode are shown in figure 4.3. The data was taken on a shot by shot basis in the QHS configuration at a plasma density of 0.9×10^{12} cm^{-3}. There is very little current drawn when the probe is biased negative with respect to the wall. In this case, the electrode current is limited by ion collection to the small cathode and a large fraction of the electrode voltage is dropped across the cathode sheath. Only a small amount of the electrode voltage is dropped over the plasma. There is substantially less voltage dropped across the electrode sheath for positive bias, and significantly more current is drawn. For this reason, positive bias is the configuration for which all further data will be reported.

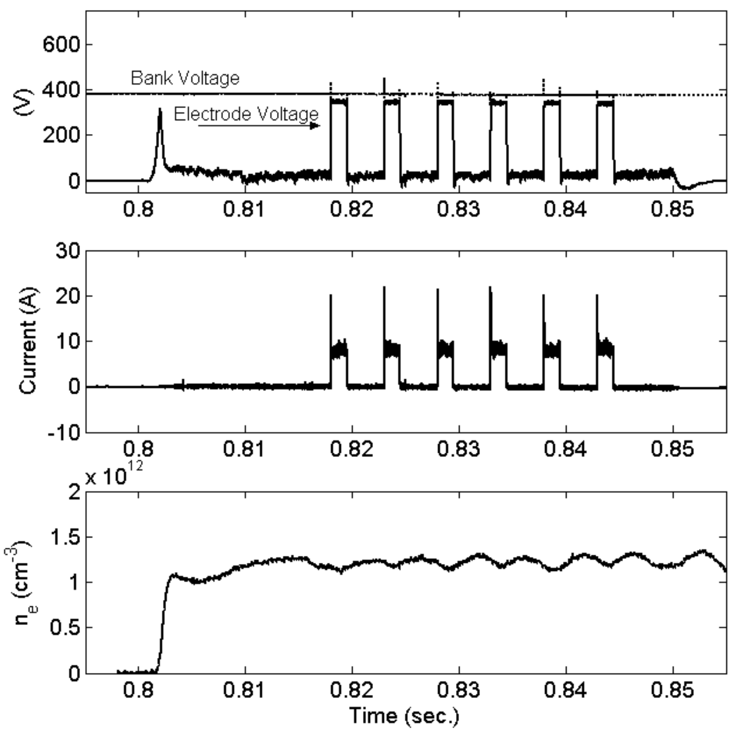

Figure 4.2: The capacitor bank and electrode voltages (top), the electrode current (middle), and the line average density (bottom) for a typical electrode biased discharge.

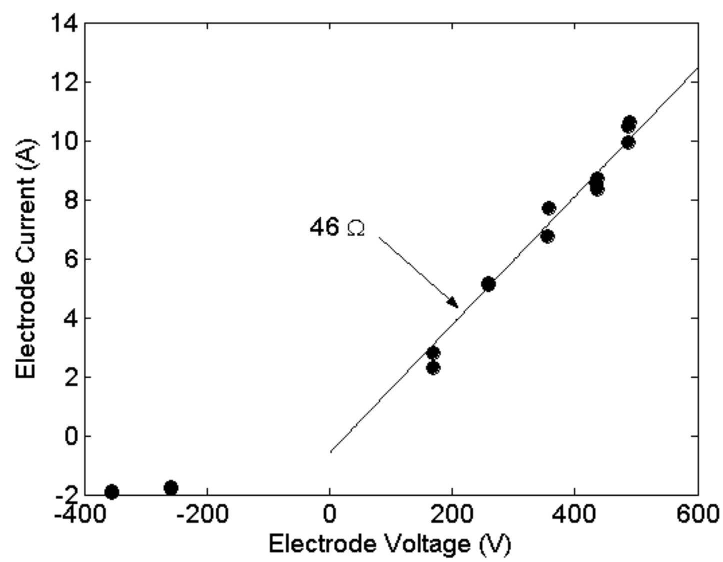

Figure 4.3: The I-V curve of the biased electrode at fixed plasma density and electrode location.

Notice that the I-V curve is a straight line, corresponding to a constant plasma resistance of ≈45Ω. This linear I-V relationship is very different from the biased H-mode cases observed in, for instance, CCT[1] and TEXTOR,[2] and indicates that if a regime of nonlinear flow damping[3,4,5] exists in HSX, then we have not yet reached that regime. This observation will provide the justification for using linear viscosities[6] in the neoclassical modeling discussed in Chapter 6. Notice that there is no sign of a rollover into electron saturation current (e_{sat}). Swept probe measurements with small probes have typically shown a rollover into e_{sat} at positive bias voltages of 200-300V.[7] Hence, it appears that the electrode current is not simply limited by electron saturation current; an explanation of this will be given shortly.

In order to determine the dependence of the electrode current on the electrode location, the biased electrode position was scanned on a shot by shot basis from outside the separatrix to inside the separatrix, with the scan ending when the electrode was at r/a≈0.6. The experiment was done in both the QHS and 10% Mirror configurations. The line average density was 1x10^{12} cm^{-3}. The result for this experiment is shown in figure 4.4, where the position of the probe is denoted by the distance from the vessel wall.

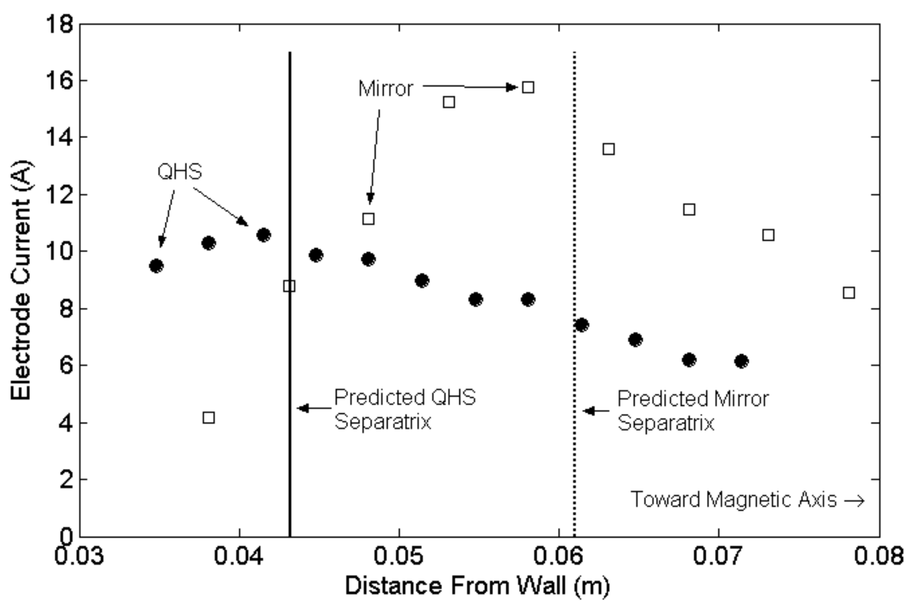

Figure 4.4: Electrode current as a function of probe location.

Based on field line following to determine the last closed magnetic surface (LCMS) and engineering drawings of the vessel, the predicted distance from the QHS and 10% Mirror separatrices to the wall are .043 and .061 meters, respectively. This plot shows that the current peaks near the predicted separatrix for both the QHS and Mirror configuration, and decreases significantly as the electrode is moved in. This is the opposite behavior of what would be seen if the electrode current was limited by electron saturation current (e_{sat} is proportional to the electron density). As an alternative explanation of this curve, consider the case that the current is limited by cross field transport. In this case each magnetic surface which the return current must cross adds some "series resistance" to the total current path. The current would then decrease as the probe is moved in, consistent with the experimental findings. This understanding of the data will be pursued extensively in the theory/experiment comparisons of radial conductivity in Chapter 7.

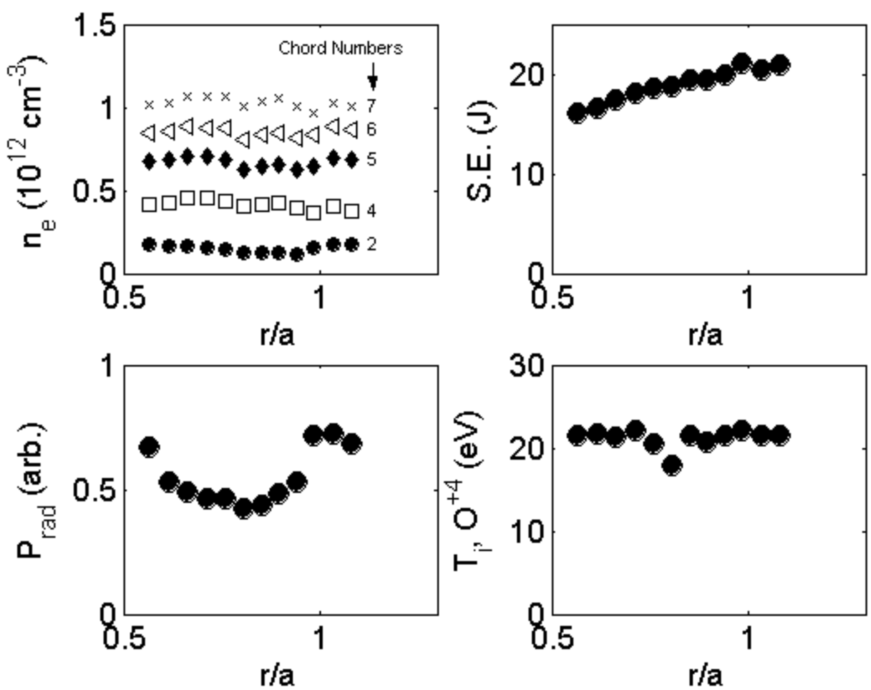

Figure 4.5: Dependence of the line average density, stored energy, radiated power, and impurity ion temperature on the electrode location.

The perturbation to the macroscopic plasma parameters as the electrode is inserted is shown in figure 4.5. The top left frame shows five chords of the interferometer. The signals are all approximately constant as a function of the electrode position, although the HSX operator was targeting the density in only chord seven as a control. Hence, we infer that there are no large changes in the density profile as the probe is inserted. In particular, the electrode does not act as a limiter.

The stored energy (top, right) exhibits a drop as the probe is inserted, losing about 30% of its value; the presence of the electrode does detrimentally impact the energy content of the plasma. The majority of stored energy in these ECH discharges is carried by electrons. It is not well understood what fraction of the electron energy may be stored in a high energy tail of the distribution function and what fraction is contained in a Maxwellian bulk. Thus, it is unclear if the large electrode is simply suppressing a distribution function tail as it is inserted, or if the bulk electron temperature is decreasing.

The radiated power (bottom, left) has one peak at the location of maximum electrode current when the electrode is located at the edge, and then a second peak as the electrode in inserted farther into the plasma. The O^{+4} brightness (not shown) roughly follows the radiated power as measured by the bolometer. The bottom right frame illustrates that the O^{+4} temperature is roughly constant over this scan. Given the constancy of these parameters, we infer that the reduction in electrode current as the probe is inserted is not due to any degradation of the plasma.

4.3 The Macroscopic Characteristics of Biased Discharges

Most biased electrode measurements in the past have concentrated on the changes in macroscopic plasma parameters, transport, and turbulence when the electrode voltage is applied.[1,2,8,9,10,11] The focus of this dissertation will be the changes in flows and electric fields when the bias is applied. The discussion of the density, recycling, and radiated power evolution over the electrode voltage pulse is limited to this section.

For most data presented for the plasma parameter evolution over a bias pulse, the signals have been averaged over many similar bias pulses. In a typical discharge, there are 4 to 6 short pulses of the biased electrode voltage. For each measurement location, two or more similar discharges are taken. Hence, it is possible to average the measured plasma evolution over 8 to 24 bias pulses. Unless otherwise noted, the data presented throughout this work will be averaged this way. When this has been done, the time axis will be shifted so that t=0 corresponds to the beginning of the electrode pulse.

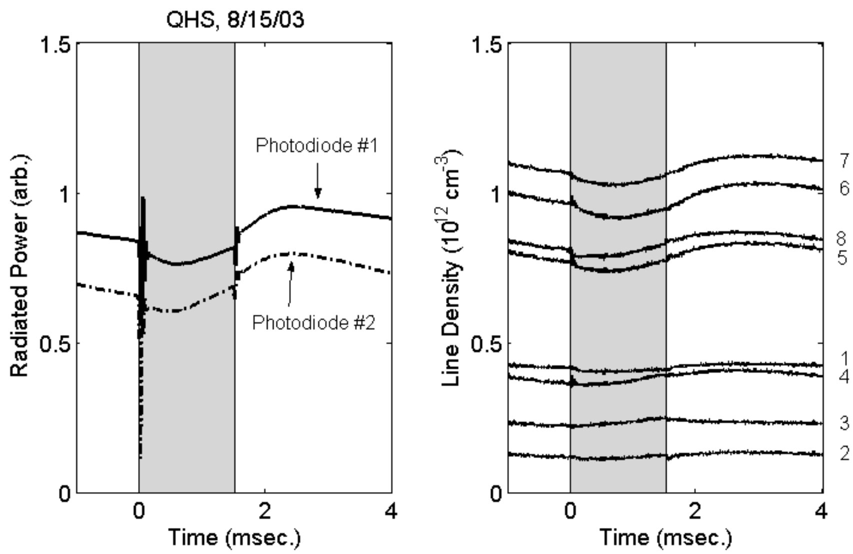

Figure 4.6: The behavior of the radiated power (left) and line average density (right) over the bias pulse, in the QHS configuration with a bias voltage of 350V and a line density of $1x10^{12}$. The number on the right denote the interferometer chord number

To begin the study, consider first the details of a set of discharges where the electrode was located at r/a≈0.65, biased to a voltage of 350V in discharges with a line average density of $1x10^{12}$ cm^{-3}. The evolution of the 9 interferometer channels and the two bolometers is shown in figure 4.6. The duration of the electrode pulse is indicated by the shaded region. There is a decrease in the density at the beginning of the bias pulse, followed by a density rise. If the bias pulse was left on for longer and the external gas feed not significantly reduced, this rise would continue all the way to ECH cutoff. The radiated power from two bolometers is shown on the left; the calibration factor has not been applied to the data for either diode. The P_{rad} dependence is very similar to the density dependence. Hence, it can be inferred that in these discharges, the energizing of electrode itself does not cause an increase in impurities.

In order to improve the understanding of the density behavior, it is useful to manipulate the data in such a way as to emphasize the change over the bias pulse. One such calculation is to divide each density waveform by its value before the bias, and then subtract 1 from this ratio. The figure of merit is thus

$$\frac{n_e(t)}{n_e(-.001\text{sec.})}-1.$$

The quantity is plotted in figure 4.7 for the different chords of the interferometer, where the various traces have been shifted up or down so that they do not overlap. The processing has the effect of emphasizing the evolution of the density during the bias pulse. The physical locations of the interferometer[12] chords are illustrated in figure 4.8. Channels #1 and #2, which pass through the plasma outside of the last closed flux surface, show a drop in density during the bias. The edge channels (3 and 4) show a steady density rise during the pulse, while the more central channels have a density drop followed by a rise.

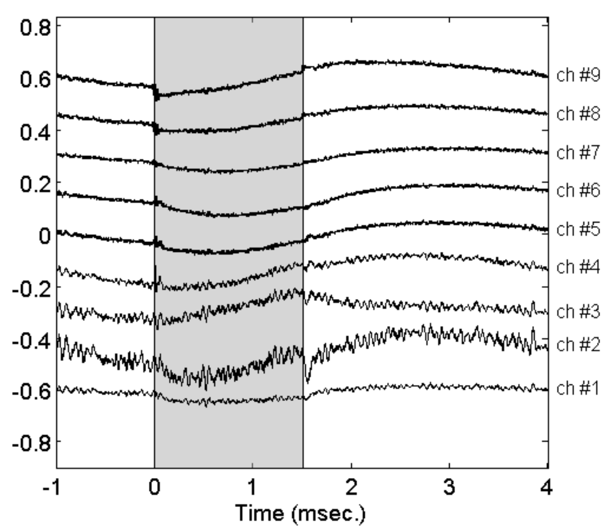

Figure 4.7: The relative changes in the density over the bias pulse, in the QHS configuration with a bias voltage of 350V and a line density of 1x10^{12}.

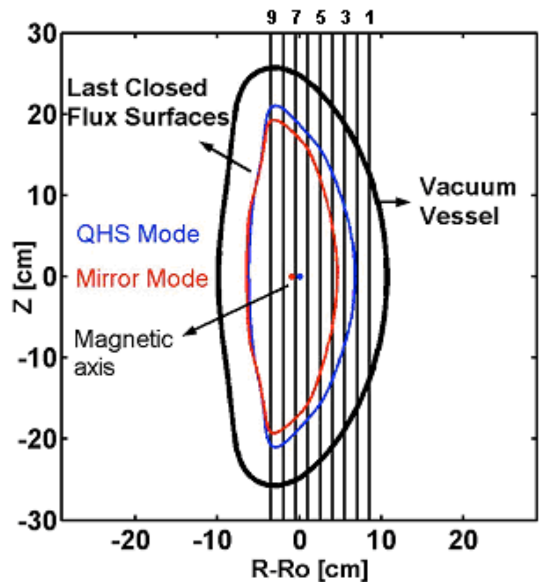

Figure 4.8: Physical Location of the interferometer chords, along with the QHS and Mirror LCMS. Figure courtesy of C. Deng.

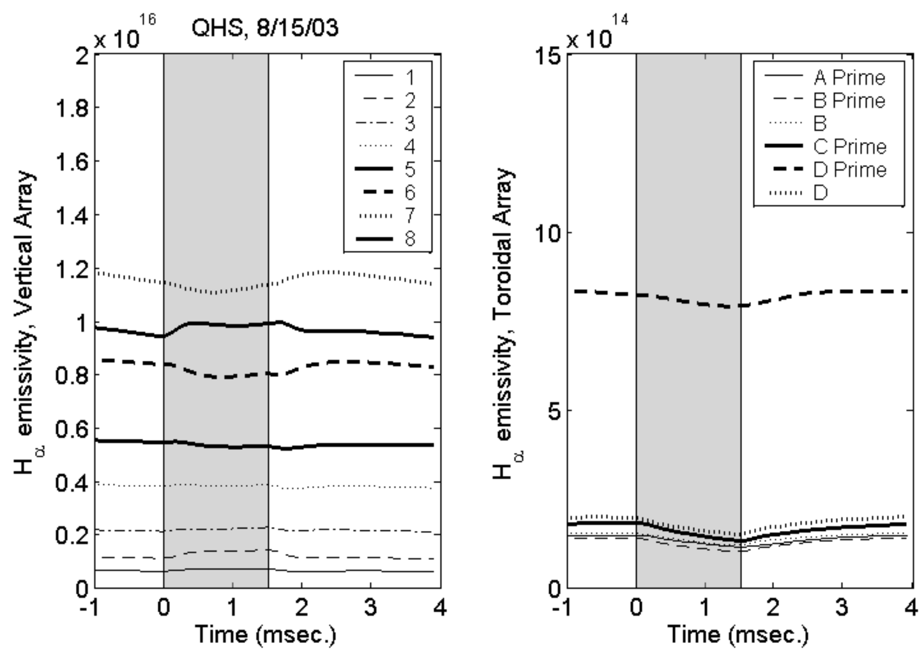

Figure 4.9: Dependence of the H_α signals over the bias pulse, in the QHS configuration with a bias voltage of 350V and a line density of $1\mathrm{x}10^{12}$.

The behavior of the H_α signals over the bias pulse is shown in figure 4.9, where the data from the poloidal array at the puffer is shown on the left and the toroidal array is shown on the right. The H_α emission at the poloidal array (left) is mostly determined by the gas puff, and hence shows a small change when the electrode is energized. The signals in the toroidal array (right frame of figure 4.9) are dominated by recycling. All of these signals drop during the bias pulse, indicating a reduction in recycling. The signal standing out in this plot is the level in field period D Prime, where the electrode resides. This signal would normally be at the level of the other detectors; some recycling occurs from the electrode, but that the level of the electrode recycling in these discharges does not significantly change when the electrode voltage is applied.

From the data presented here, it occurs that there may be some improvement in particle confinement during the bias pulse in the QHS mode. There is a reduction in recycling, a decrease in the SOL density, and an increase in the edge density. Furthermore, evidence will be presented in Section 4.6 that there is a reduction in turbulence with the electrode pulse.

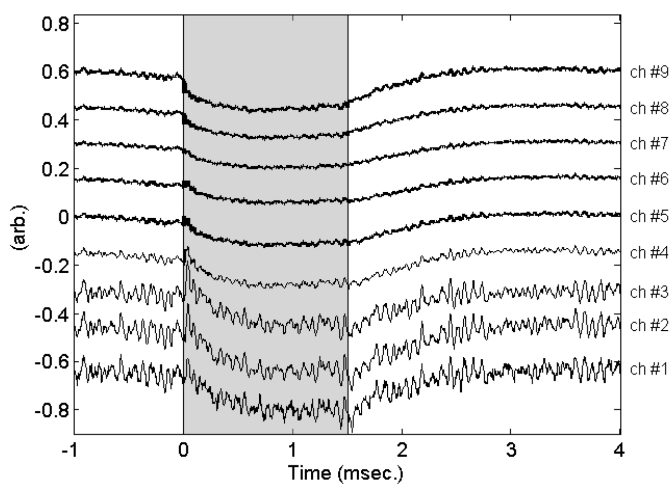

Figure 4.10: The relative changes in the density over the bias pulse, in the QHS configuration with a bias voltage of 500V and a line density of $1x10^{12}$.

The phenomenology associated with the density evolution and recycling during the bias pulse appears to be quite complicated. As an example, the relative change in the density for discharges similar to that presented above, but with an electrode voltage of 500V, is shown in figure 4.10. In this case, the density in all channels drops during the bias pulse. The H_α signals behave in a manner similar to the case above, although the radiated power rises throughout the bias pulse.

The bulk plasma behavior in the Mirror configuration also appears to be different than in the QHS configuration. In Mirror discharges at a density of $1x10^{12}$ cm^{-3} and a bias voltage of 350V applied at r/a=.7, the H_α behavior is similar to the equivalent QHS case. The density in all of the interferometer channels drops throughout the bias voltage pulse, and the radiated power rises throughout the electrode pulse.

In general, it appears to be difficult to make a unified picture of the density, radiated power, and recycling behavior during the electrode pulse. Most likely, the recycling conditions of both the electrode head and the vacuum vessel walls are important factors in these studies. Further, the recycling may be different for the QHS and Mirror configurations. Note that the discharges presented here are limited to short (1.5msec.) bias pulses to minimize these perturbations. Longer electrode voltage pulses are probably required to establish more clearly the macroscopic confinement trends. These longer bias pulse discharges will need their gas feed reduced in such a fashion as to avoid a density run away. This type of experiment can be done, although it is much more difficult than simply using short bias pulses.

One important observation is clear from these studies. When the electrode is sufficiently clean and the voltage pulse width is kept sufficiently short, there are only small perturbations to the plasma density and particle transport dynamics. The neutral and electron densities appear to change by <20% under these conditions. These are important considerations when considering the electric field and plasma flow evolution discussed in the next section.

4.4 The Phenomenology of the Electric Field and Biased Flow Evolution

When the biased electrode is energized, there are significant changes in the electric field and plasma flows. The general phenomenology of the plasma flow and electric field behavior is discussed in this section. In each case, example data will be presented for the QHS configuration first; Mirror configuration will be discussed afterward in some cases. Comparisons with modeling will be made in Chapter 7, once the theory behind the modeling has been introduced in Chapters 5 and 6.

This chapter is divided into two sections. Section 4.4.1 illustrates the steady state profiles of the plasma flow and floating potentials, both before and during the electrode bias. Measurements are shown from the high and low field sides of HSX, as well as at different densities and in both the QHS and Mirror configurations. Section 4.4.2 provides details of the time evolution of these parameters. The plasma response at bias turn-on and turn-off is described in detail. Data analysis methods are introduced that allow the extraction of multiple time scales from the data.

4.4.1: Profiles of the Floating Potential, Electric Fields, and Plasma Flows in Electrode Biased Plasmas.

Typical profiles of the floating potential (V_f) in the QHS configuration are shown in the top frame of 4.11, where the profiles have been measured by moving the low field side (LFS) Mach probe on a shot to shot basis. As anticipated, there is a large increment in the floating potential when the bias is on. Note that the data is plotted against the distance from the last closed magnetic surface (LCMS). The biased electrode is on a surface corresponding to ~2.75cm in this figure.

The radial electric field is calculated by differentiating the floating potential with respect to the distance along the axis on which the probe moves, and is denoted as dV_f/dl. The electric field so calculated is shown in the bottom frame of figure 4.11, with calculations for both before and during the bias pulse. The electric field has a peak at $\approx$1cm inside the separatrix with a magnitude of ~10kV/m.

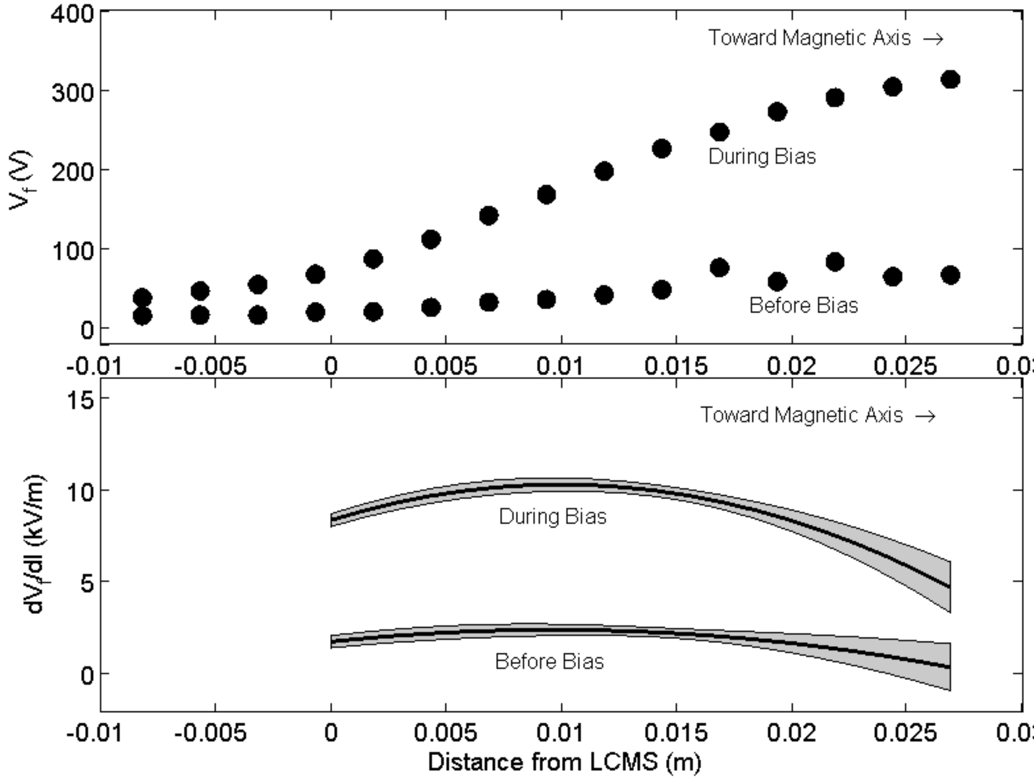

Figure 4.11: Profiles of the floating potential (V_f) before and during electrode bias (top), and the associated electric field (bottom), for the QHS configuration on the low field side.

This electric field calculation is based on floating potential measurements, instead of more appropriate plasma potential measurements. The plasma potential is given by $V_p=V_f+\kappa T_e$, where κ is a plasma species dependent parameter. By calculating the electric field from the floating potential only, possible ∇T_e corrections are omitted. In QHS discharges without probes, Thomson scattering measurements show a relatively flat electron temperature profile in the outer 1/3 of the plasma cross section.[13] Measurements with single and double swept Langmuir probes have indicated a flat T_e profile in the edge with a value of ~40 eV.[14] Hence, it may be the case that the ∇T_e correction to the floating potential measurement is not large. In any case, the large floating potential gradient during the electrode bias reduces the significance of ∇T_e corrections during the electrode pulse.

A second consideration with this electric field calculation comes with regard to the differentiation variable. If the axis along which the probe is inserted is not orthogonal to the magnetic surfaces, then this calculation would underestimate the radial electric field. The magnetic surfaces and probe insertion axes were illustrated in figure 2.6. The figure shows that in both cases, the probe axis is close to orthogonal to the magnetic surfaces. More importantly, the rigorous theory/experiment comparisons illustrated in Chapter 7 rely on differentiation of the potential with respect to toroidal flux. Using toroidal flux as a surface label eliminates this ambiguity in the radial coordinate.

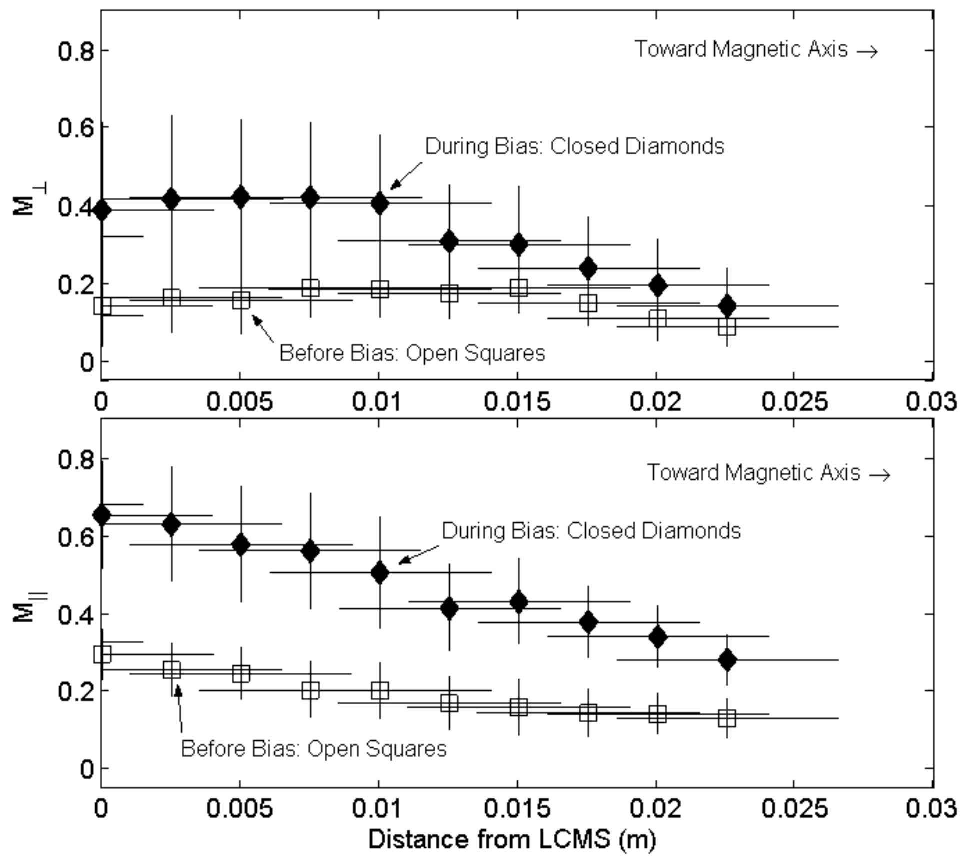

Figure 4.12: Profiles of the perpendicular (top) and parallel (bottom) Mach numbers as a function of distance from the last closed magnetic surface on the low field side, for the QHS configuration.

The steady state flow profiles for the same discharges (QHS, 1×10^{12} cm^{-3}) are shown in figure 4.12. The data is displayed as broken into perpendicular (top) and parallel (bottom) flows, where the directions are referenced to **B**. During bias, the perpendicular flows have the same radial profile as does the electric field: there is a peak at ≈ 1cm inside the separatrix, and then a decrease toward the plasma center. Note the large increment in the parallel flow during bias.

The dominant source of error in this measurement is the systematic error in the determination of the angular calibration of the probe with respect to the magnetic field. For example, if the flow is mostly parallel, then small errors in the angle calibration will lead to large errors in the perpendicular flow. This is directly analogous to, for instance, the problem of coil alignment errors in the measurement of the poloidal magnetic field in a device with a strong toroidal magnetic field.

In relationship between the perpendicular flows and electric fields is given by the radial force balance equation

$$\mathbf{E}_r + \mathbf{V} \times \mathbf{B} = \nabla p \,. \tag{4.1}$$

This equation must be satisfied for every species independently, at all points in the plasma. Neglecting the ion temperature gradient, the ratio of the ion pressure gradient to electric field during electrode bias can be worked out as:

$$\frac{\nabla p}{E_r} \sim \frac{N_i T_i}{\Phi} \frac{L_\Phi}{L_N} \sim \frac{1x10^{18} 1.6x10^{-19} 20}{300} \frac{.03}{.06} \approx 5x10^{-3}$$

With this justification for neglecting the ion pressure gradient, the final two terms of the force balance during bias (absolute value shown) are illustrated in figure 4.13.

In making this comparison, the sound speed (defined by Hutchinson as c_s=sqrt(T_e/m_i))[15] is computed assuming a flat electron temperature profile of 40eV with an uncertainty of 20eV. The vertical error bars represent errors in both $M_\perp$ and c_s. Errors in the Hutchinson model calibration factors (k_u and k_d in equation (2.7)) are not known and so cannot be included in the figure. The agreement with force balance appears to be reasonably good.

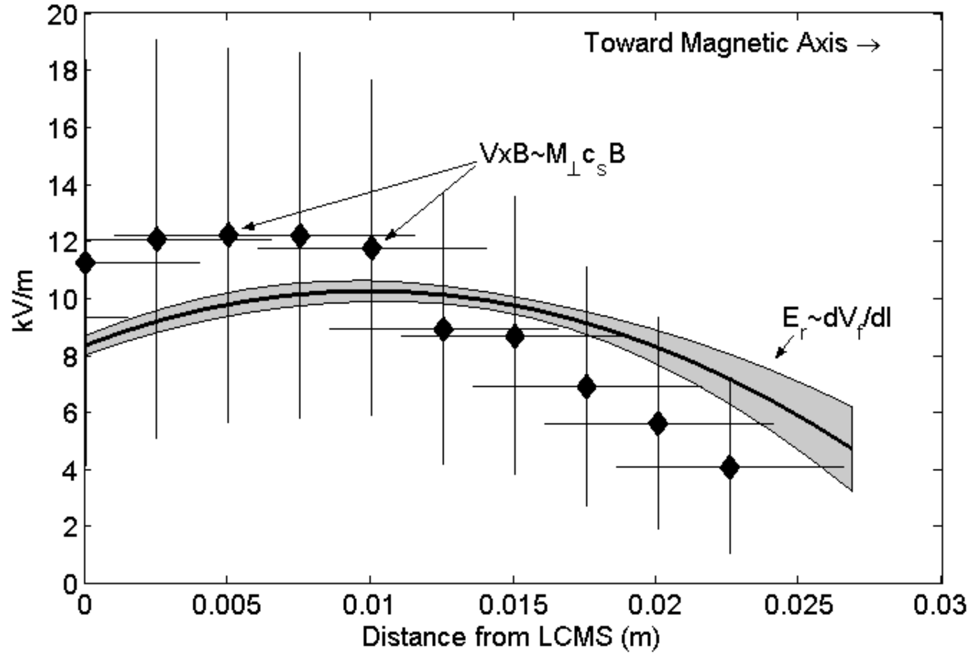

Figure 4.13: Comparison of radial force balance on the low field side in $1x10^{12}$ cm^{-3} QHS plasmas.

Similar measurements have been made for the Mirror configuration, also at a density of $1x10^{12}$ cm^{-3}. The floating potential and electric field data are shown in figure 4.14. The trends are similar to the QHS configuration, although the electric field is somewhat larger at the edge and smaller at locations farther in.

The profiles of the parallel and perpendicular Mach numbers in the Mirror configuration are shown in figure 4.15. These discharges have a line average density of $1x10^{12}$ and are as similar to the previously discussed QHS discharges as experimentally possible. Note that there is not a large increment in the parallel flow during bias, unlike in the QHS configuration.

The radial force balance comparison for these Mirror discharges is illustrated in figure 4.16. The agreement is once again reasonably good.

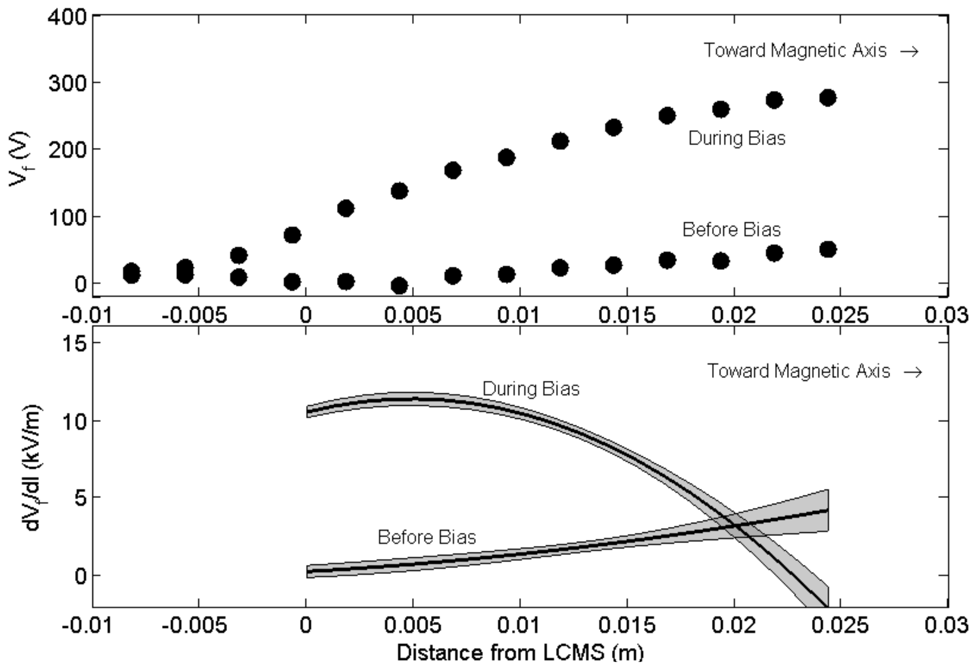

Figure 4.14: Profiles of the floating potential (V_f) before and during electrode bias (top), and the associated electric field (bottom), for the Mirror configuration on the low field side.

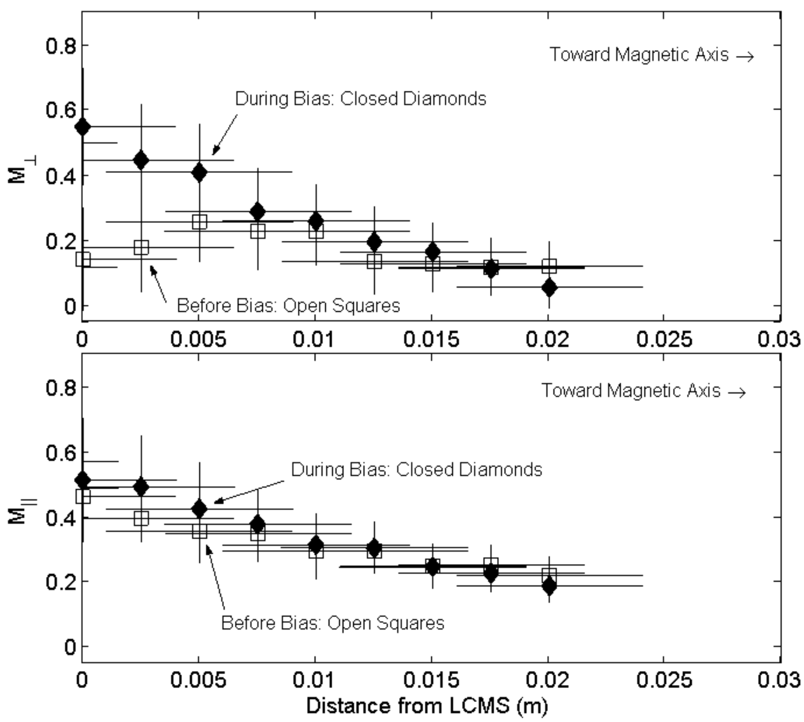

Figure 4.15: Profiles of the perpendicular and parallel Mach numbers as a function of distance from the last closed magnetic surface, for the Mirror configuration on the low field side.

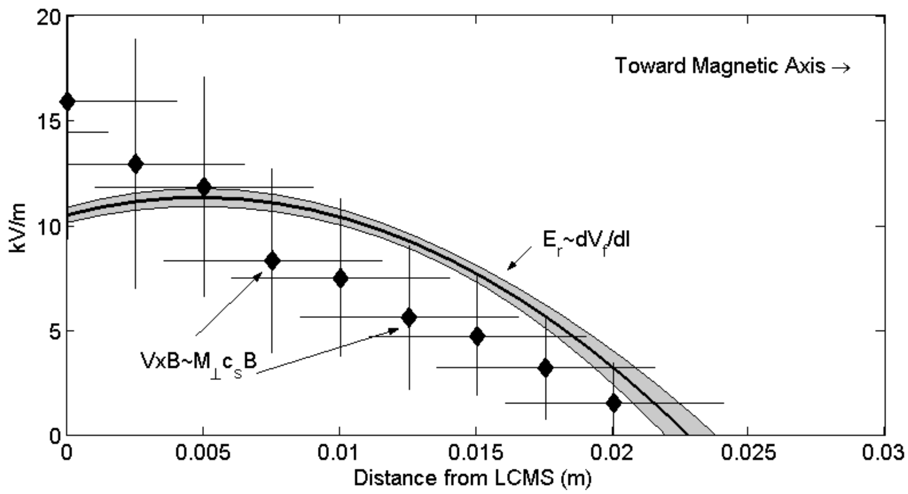

Figure 4.16: Comparison of radial force balance on the low field side in 1×10^{12} cm^{-3} Mirror plasmas.

Recall that there are two Mach probes on HSX: one on the low field side of the torus and one on the high field side. Similar electric field and flow studies have been done with the high field side Mach probe. The electric field data is illustrated in figure 4.17. The insertion location for the high field side probe has it going into the end of the triangular cross section, where the flux surfaces are more extended (see figure 2.6). For a fixed distance inside the last closed surface, this probe will be at a larger value of toroidal flux than the low field side probe. This is the reason that the floating potential has only gone to 180V at 3cm inside the LCMS, compared to 300 V for the low field side probe.

The profiles of the plasma flow for the high field side probe are displayed in figure 4.18. During bias, the Mach number of the perpendicular flow is approximately half of what it is on the low field side (0.2 compared to 0.4). The electric field during bias is also half of the value on the high field side (4kV/cm compared to 8kV/cm), due to the expansion of the flux surfaces at this location. The radial force balance (not shown) thus works out correctly for this data as well. There is a large increment in the parallel flow during the electrode voltage application, as noted in the QHS low field side measurements.

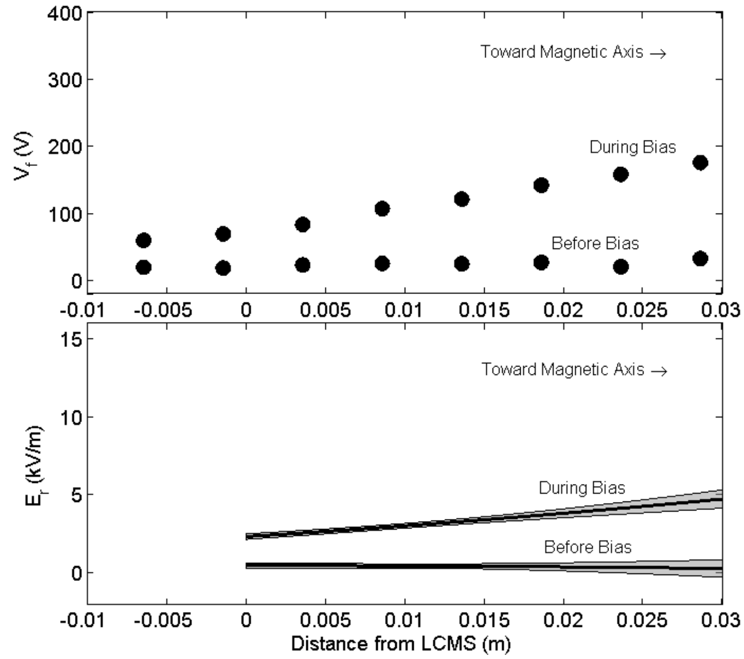

Figure 4.17: Profiles of the floating potential before and during electrode bias (top), and the associated electric field (bottom), for the QHS configuration on the high field side.

The satisfaction of radial force balance before bias is not so clear. The electric field as inferred from the floating potential measurements is essentially zero, yet there is perpendicular flow with Mach number ~0.2. More studies need to be made to understand the radial force balance in unbiased plasmas. Proper inclusion of ∇T_e effects in the electric field measurement are warranted, and inclusion of the ion temperature gradient in the pressure gradient term may be important.

Throughout this study, it will be important to compare measurements made with Mach probes on the high field side (HFS) and low field side (LFS) of HSX. To facilitate this measurement, the data for each probe is mapped from physical probe location to an r/a coordinate (r/a=sqrt($\psi/\psi_{boundary}$), with ψ the toroidal flux). The values of r/a outside the LCMS are extrapolated from values inside the LCMS.

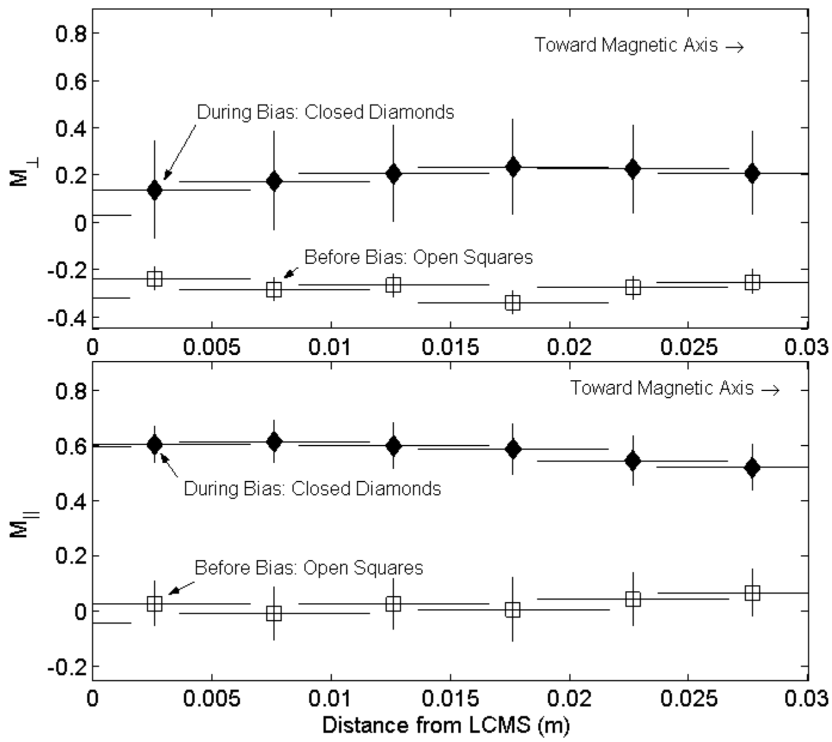

Figure 4.18: Profiles of the perpendicular and parallel Mach numbers as a function of distance from the last closed magnetic surface, for the QHS configuration on the high field side.

The LFS and HFS profiles of V_f measured for 350V bias are shown in figure 4.19, with the radial locations of both probes mapped to flux coordinates. The potential profiles overlap very nicely, both before and especially during bias. While this may not be enough evidence to strictly claim that the potential is a flux surface constant, it shows that the potential is similar at two very different measurement locations (~135° toroidal separation). Note that the r/a values outside the LCMS, based on extrapolation from calculations inside the LCMS, do not provide a reasonable means to compare data taken at different locations outside the LCMS.

These floating potential profiles change very little with density. The profiles from the LFS probe are shown in figure 4.20, for discharges with line average densities of 5×10^{11} cm^{-3} and 1×10^{12} cm^{-3}. The data has been mapped to normalized minor radius. The profiles of the floating potential during bias are virtually identical, although the unbiased floating potential is slightly higher at lower density. The electrode current changes from I_{bias}= 2.75 A for the low density case to I_{bias}= 7A for the high density case. The implied density scaling of the radial conductivity will be discussed in more detail in Chapter 7.

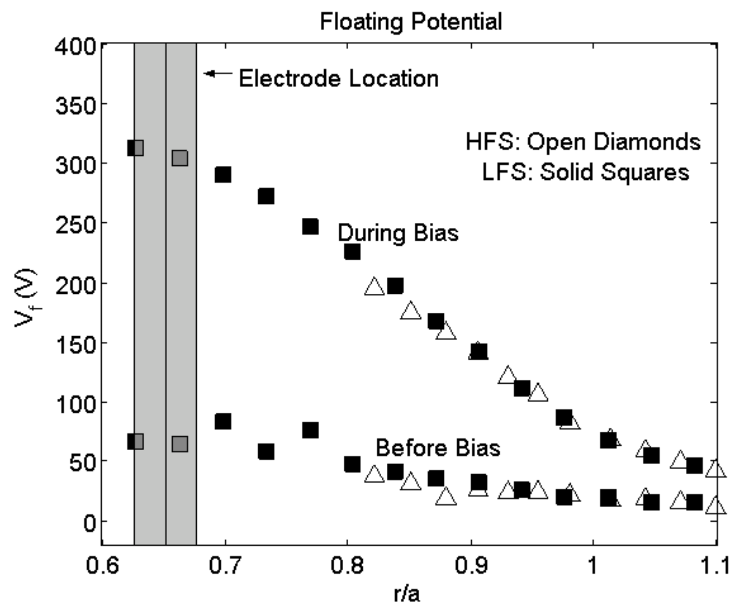

Figure 4.19: Profiles of the floating potential (V_f) measured on both the high field and low field side of the HSX.

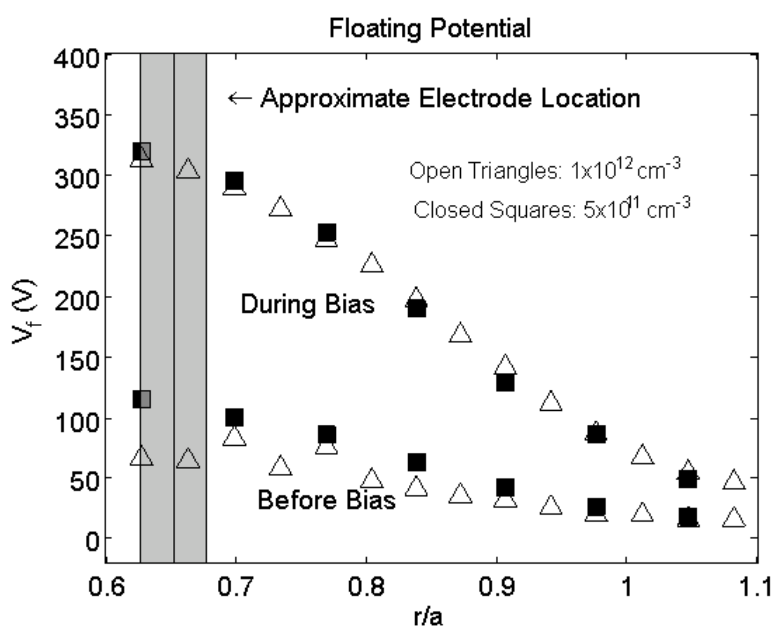

Figure 4.20: Profiles of the floating potential (V_f) measured on the LFS, for line average densities of $1x10^{12}$ cm^{-3} and $5x10^{11}$ cm^{-3}.

The profiles of the flows during bias are illustrated in figure 4.21, for the two densities compared in figure 4.20. Just as the floating potential profiles are very similar, the perpendicular flow profiles are very similar. The parallel flow during bias is somewhat higher at the lower density.

To finish this section, consider a comparison of the steady state floating potential profiles in QHS and Mirror configurations, when radial locations both have been mapped to flux coordinates. These profiles were illustrated in figures 4.11 and 4.14 above, and have been mapped to flux coordinates in figure 4.22. Detailed radial conductivity studies based on these profiles will be discussed in Chapter 7.

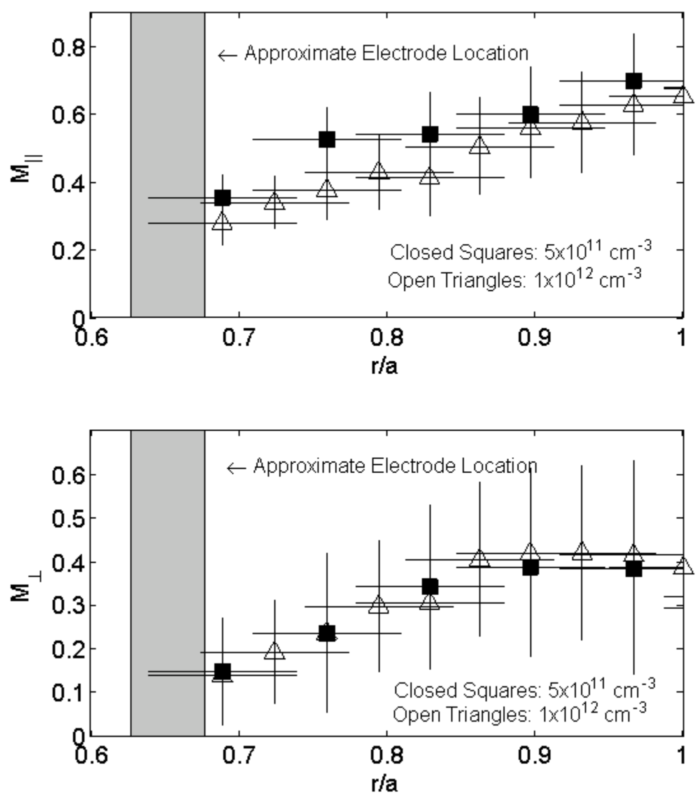

Figure 4.21: Profiles of parallel and perpendicular Mach numbers during bias, for densities of $1x10^{12}$ cm^{-3} and $5x10^{11}$ cm^{-3}, in the QHS configuration.

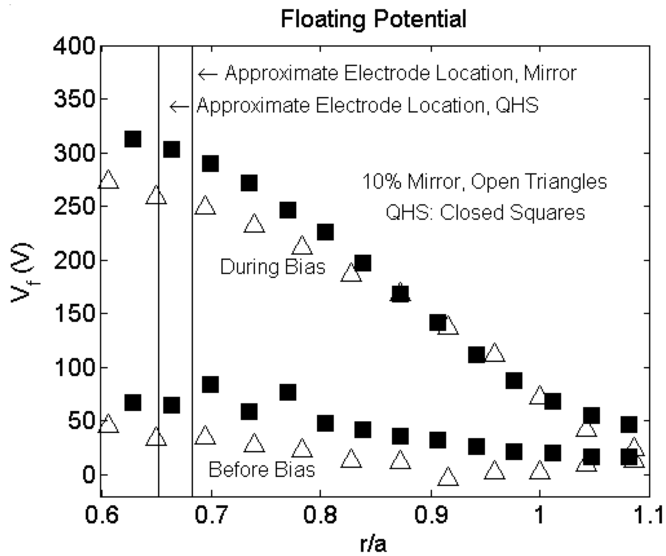

Figure 4.22: Floating Potential profiles in the QHS and 10% Mirror configurations, for n_e=1x10^{12} cm^{-3}.

This data also shows that under these conditions (1x10^{12} cm^{-3} plasma density), the floating potential before bias is higher in the QHS configuration than the Mirror. It is important to remember that the "before bias" data still has the large electrode sitting well inside the LCMS. This electrode leads to some degradation of plasma parameters. Hence, it should not be inferred that the plasma properties "before bias" are the same as in discharges without the electrode. Detailed measurements of flows and electric fields in unbiased plasmas should be conducted as a separate step.

4.4.2: Time Evolution of the Electrode Characteristics, Floating Potential, and Plasma Flows.

The evolution of the electrode voltage and current over a bias pulse is shown in figure 4.23. Note that the voltage rises very quickly when the electrode is energized and stays constant throughout the bias pulse. The electrode current has a large spike at the beginning of the voltage pulse before settling at a steady value. On the other hand, the current is turned off very quickly at the end of the pulse, while the electrode voltage decays with a time constant of ~40 μsec. From these graphs alone, it can be observed that the turn-on and turn-off of the electrode are not simply mirror images of each other.

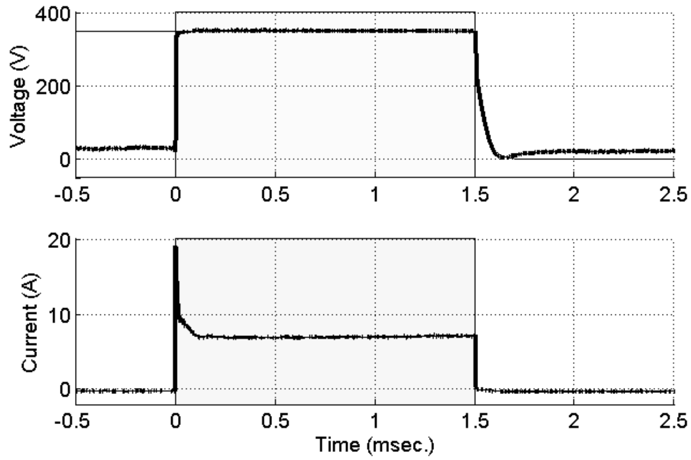

Figure 4.23: Detail of the electrode voltage (top) and electrode current (bottom) evolution over the duration of the electrode voltage pulse.

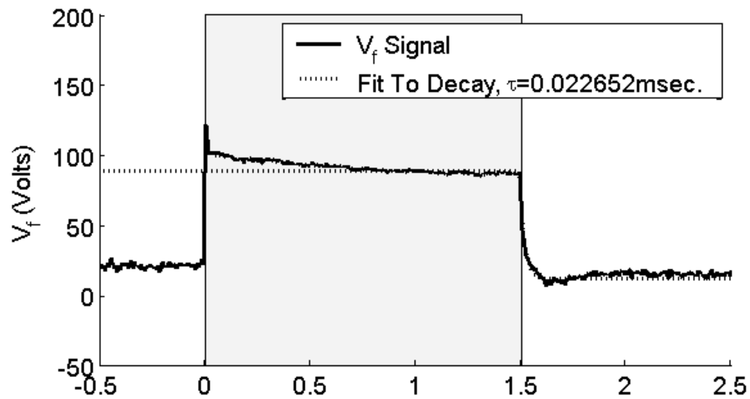

Figure 4.24: Evolution of the floating potential (solid line)over a bias pulse. The exponential fit to the decay is also shown (dashed).

This asymmetry between the turn-on and turn-off is also seen in the evolution of the floating potential, as shown in figure 4.24. This is a QHS discharge with a line average density of $1x10^{12}$ cm^{-3}; the biased electrode is at r/a≈0.65 and the measurement probe is at r/a≈0.85. There is an almost instantaneous rise in the floating potential when the electrode is energized. The decay, however, occurs on a time scale of 20-50μsec, as indicated by the dotted line in the figure.

This rise/fall asymmetry of the potential evolution will be an important feature in the modeling discussion of Chapter 5.

The evolution of the 6 Mach probe signals over the electrode pulse is shown in figure 4.25, for the same probe and shot numbers as the floating potential evolution in figure 4.24. The shaded region indicates the duration of the bias pulse. The separation of the six signals during the bias pulse is indicative of increasing plasma flows, as shown in Chapter 2. Hence, it is apparent that the plasma is flowing more quickly during the duration of the bias pulse than before or after.

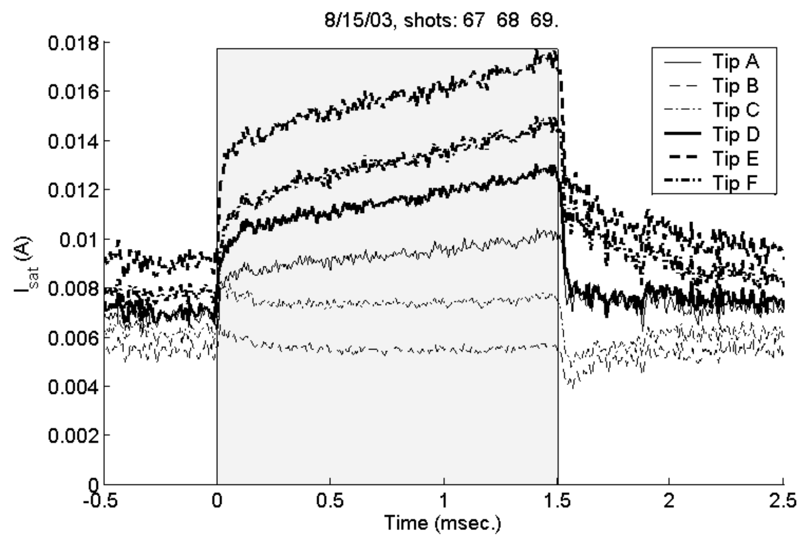

Figure 4.25: Evolution of the six I_{sat} signals from Mach probe 1 (LFS) over a typical bias pulse.

As described in Chapter 2, this data is analyzed at each point in time using the Hutchinson Mach probe model,[15] yielding a time history of the flow evolution. These fits at 9 times between 0 and 0.5msec. are shown in figure 4.26. The increase in flow is indicated by the points shifting up and to the left as time goes by and the plasma accelerates. Note that at each point in time, the fit and the data agree well. The angle variable has an arbitrary rotation with respect to **B** in this plot.

The time history of two of the fit parameters is shown in figure 4.27, where the Mach number and angle of the flow are plotted over the duration of the bias pulse. The flow speed evolution after the electrode is turned on or off is clear. Note that there is also some small evolution in the flow angle.

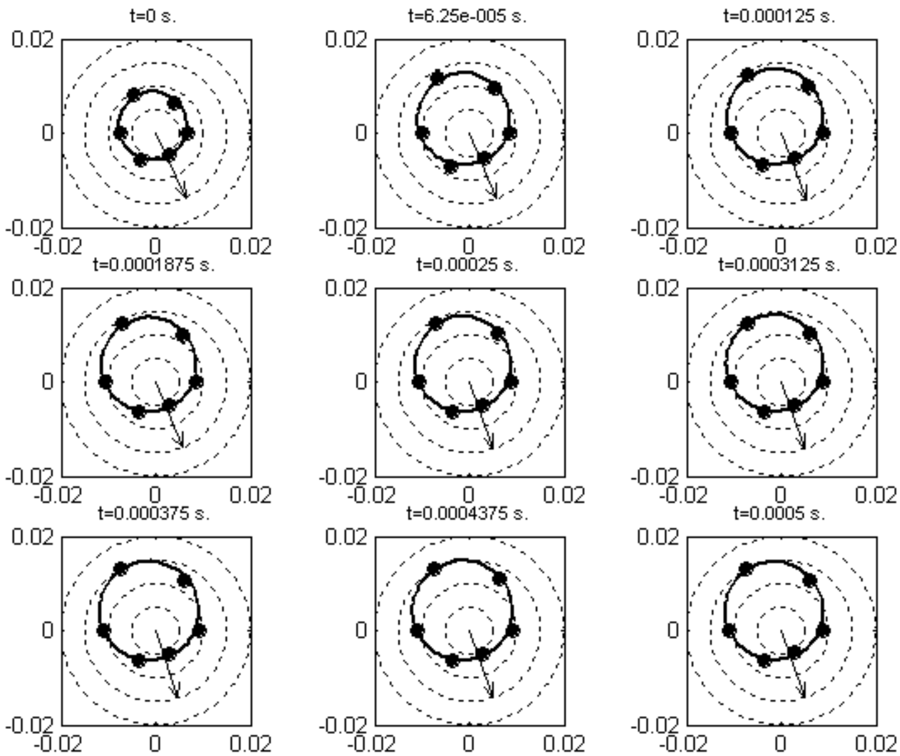

Figure 4.26: Fits of the Hutchinson model to the I_{sat} data at different points in time during the flow spin-up.

Chapter 6 will show that neoclassical theory predicts there to be two time scales in the evolution of the flow speed. This is true for both the spin-up and relaxation of the flows. There will be a direction associated with each time scale, so that the steady state flow is the vector sum of the flow in these two directions. It is thus necessary to analyze the flow evolution data so that multiple time scales can be extracted. The fact that two time scales are present can be seen in the data in figure 4.27, where the rise time of the flow indicates a fast rise followed by a slower rise. Furthermore, there is some evolution of the flow angle at the beginning and end of the bias pulse.

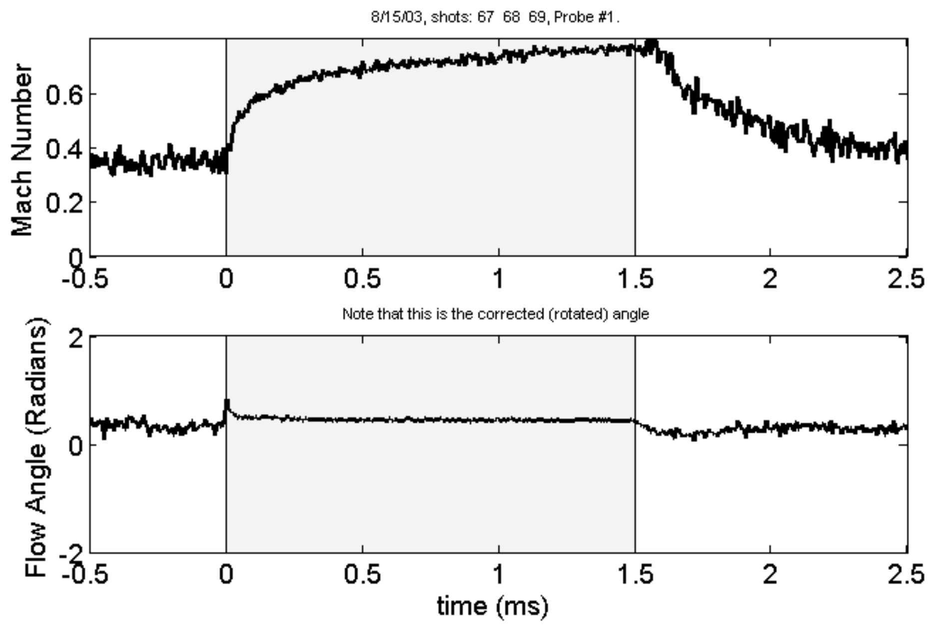

Figure 4.27: Evolution of the flow speed (top) and angle (bottom) over the bias pulse.

The fitting procedure for the flow rise proceeds as follows. The data, in the form of the flow speed and angle, is broken into two components as

$$U_{\mathbf{exp},1}(\mathrm{t}) = \mathrm{M}(\mathrm{t})\,\mathbf{cos}(\theta_f(\mathrm{t})) - \mathrm{M}_o\,\mathbf{cos}(\theta_{fo}), \tag{4.1a}$$

$$U_{\mathbf{exp},2}(\mathrm{t}) = \mathrm{M}(\mathrm{t})\,\mathbf{sin}(\theta_f(\mathrm{t})) - \mathrm{M}_o\,\mathbf{sin}(\theta_{fo}). \tag{4.1b}$$

In this expression, M_o and θ_{fo} represent the values of those parameters averaged over a window before the bias is applied. This definition of $U_{exp,1}$ and $U_{exp,2}$ has the effect of subtracting off the plasma flows which existed before the bias is applied. Note that both the plasma speed (M) and the flow angle (θ_f) are functions of time. It is the evolving flow angle which makes it necessary to use the two projections when analyzing the data. If the flow angle did not evolve, then a simple two time scale rise fit to the flow speed rise would be sufficient to extract the time scales.

The next step is to use these projections to extract the two time scales. The general vector expression for a two time scale two direction flow evolution is given by

$$\mathbf{U}_{\mathrm{fit}}(\mathrm{t}) = \begin{cases} 0 & \mathrm{t} < 0 \\ \mathrm{C_f}\left(1 - \exp\left(-\,{}^{\mathrm{t}}\!/_{\tau_\mathrm{f}}\right)\right)\mathbf{f} + \mathrm{C_s}\left(1 - \exp\left(-\,{}^{\mathrm{t}}\!/_{\tau_\mathrm{s}}\right)\right)\mathbf{s} & \mathrm{t} > 0 \end{cases}. \tag{4.2}$$

In this expression, the variables C_f, τ_f, and **f** (a unit vector) represent the magnitude, time scale, and direction of the faster evolving flow, while C_s, τ_s, and **s** represent the magnitude, time scale, and direction of the slower evolving flow. Taking the cosine and sine projections of this equation yields

$$U_{1,\mathrm{fit}}(\mathrm{t}) = \begin{cases} 0 & \mathrm{t} < 0 \\ \mathrm{C_f}\left(1 - \exp\left(-\,{}^{\mathrm{t}}\!/_{\tau_\mathrm{f}}\right)\right)\cos(\alpha_\mathrm{f}) + \mathrm{C_s}\left(1 - \exp\left(-\,{}^{\mathrm{t}}\!/_{\tau_\mathrm{s}}\right)\right)\cos(\alpha_\mathrm{s}) & \mathrm{t} > 0 \end{cases}, \tag{4.3a}$$

$$U_{2,\mathrm{fit}}(\mathrm{t}) = \begin{cases} 0 & \mathrm{t} < 0 \\ \mathrm{C_f}\left(1 - \exp\left(-\,{}^{\mathrm{t}}\!/_{\tau_\mathrm{f}}\right)\right)\sin(\alpha_\mathrm{f}) + \mathrm{C_s}\left(1 - \exp\left(-\,{}^{\mathrm{t}}\!/_{\tau_\mathrm{s}}\right)\right)\sin(\alpha_\mathrm{s}) & \mathrm{t} > 0 \end{cases}. \tag{4.3b}$$

Note that $\cos(\alpha_f)$ and $\sin(\alpha_f)$ are the projections of **f** into the orthogonal coordinate system of (4.1), and similarly for the $\cos(\alpha_s)$ and $\sin(\alpha_s)$ terms. These two expressions can be fit to the projections of the measured flow using a nonlinear fitting routine, where the parameters τ_f, τ_s, C_f, C_s, α_f and α_s are allowed to vary in the fitting routine. The figure of merit to be minimized in the fitting process is defined as

$$\chi^2 = \sum \frac{\left(U_{\exp,1}(t) - U_{1,fit}(t)\right)^2}{\sigma_{U1}^2} + \sum \frac{\left(U_{\exp,2}(t) - U_{2,fit}(t)\right)^2}{\sigma_{U2}^2}. \tag{4.4}$$

This fit yields the time scales of the flow evolution, as well as the amount of flow and direction associated with each time scale.

A detailed example of the fits is shown in figure 4.28. The large bottom plot shows the measured and fit values of U_1 and U_2. The flow angle has been adjusted so that θ_f=0 corresponds approximately to the direction of the magnetic field. The approximately perpendicular flow grows very quickly, while the parallel flow has a second longer time scale in its flow evolution. The fits to

U_1 and U_2 can be seen to fit the data very well. The two time scales for the flow rise are calculated to be 330μsec and ≈8μsec.

The top two frames illustrate the measured magnitude and direction of the flow. The fit to the speed, defined as $(U_{2,fit}^2+U_{1,fit}^2)^{1/2}$, is shown in the top frame. The fit to the angle, defined as $\tan^{-1}(U_{2,fit}/U_{1,fit})$, is shown in the center frame. Note that before the bias is applied (shaded region), the flow is near zero and the angle is poorly defined, due to the offset subtraction as described by equation (4.1).

As noted in subsection 4.4.1, there is ≈10°-15° of systematic error in the determination of the Mach probe's angle alignment with respect to the magnetic field. The decomposition of the flow into orthogonal directions in equation (4.1) makes no use of the alignment calibration; the flows are broken into orthogonal directions in a coordinate system of arbitrary rotation with respect to the magnetic field direction. The fits described in equations (4.2) and (4.3) produce angles which are in this arbitrary coordinate system. The systematic error comes in aligning these angles to the magnetic field direction. The time scales themselves are independent of the angle calibration. The fast and slow angles produced by the fits have the same systematic errors with respect to the magnetic field as the data before the fits were computed.

A note of caution is in order concerning the fast time scale measurements. This fast time scale and the direction associated with it have significant uncertainty in some cases, as the bandwidth of the I_{sat} amplifiers is only 100 kHz. It is sometimes the case that the fast fit direction from equation (4.3) does not match well with the direction of the initial rise in flow. Even with this caveat, it is clear that there is a fast and a slow component to the rise, and that the slow time scale is easily within the limits of the measurement instruments. This 2 time/2 direction technique generally converges to reasonable estimates of the slower rise time and the direction associated with the slower rise.

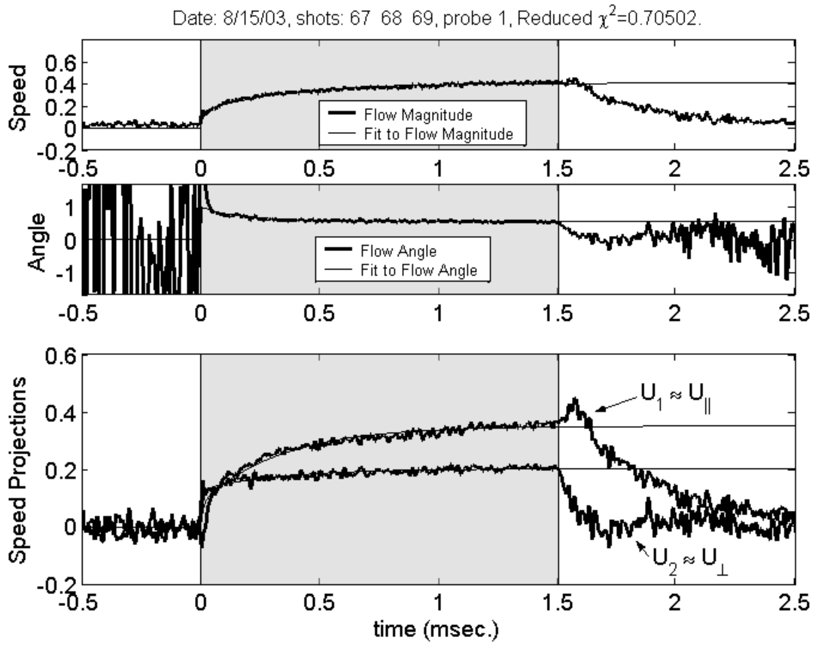

Figure 4.28: Evolution of the flow speed (top) and angle (middle) over the bias pulse, along with the flow projections (bottom) and the fits to the flow rise, for the low field side (LFS) Mach probe in the QHS configuration.

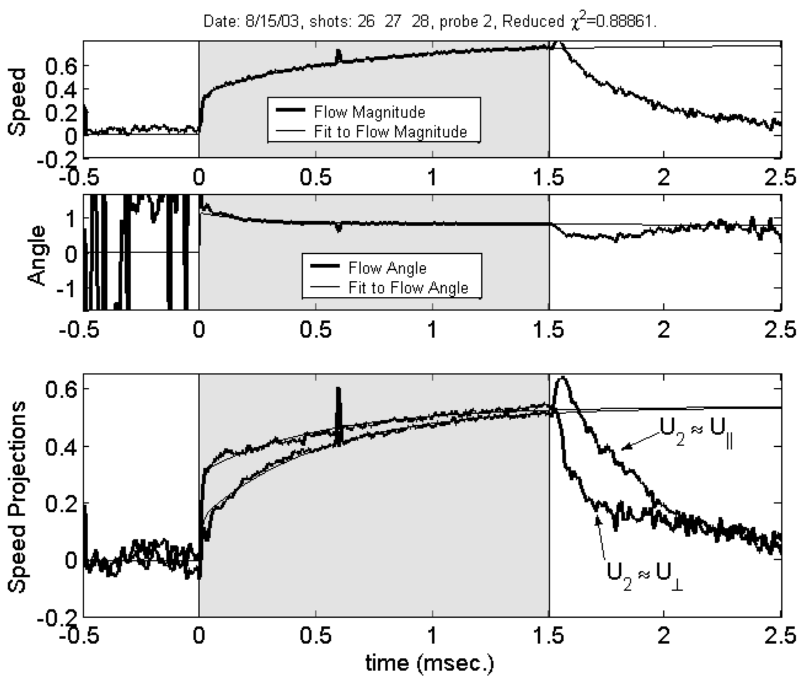

Figure 4.29: Evolution of the flow speed (top) and angle (middle) over the bias pulse, along with the flow projections (bottom) and the fits to the flow rise, for the high field side (HFS) Mach probe in the QHS configuration.

As a second illustration of the measurement, a similar plot is shown in figure 4.29 for data taken with the high field side Mach probe. Similar trends are evident in the data. The perpendicular flow rises very quickly, while the parallel flow grows more slowly, illustrating the two time scale nature of the flow.

The convergence of this fit is equally good in the Mirror configuration. There is typically a larger fraction of the flow in the fast direction for the Mirror configuration, enabling the fast direction to be better resolved in some instances. An example of the fit for the Mirror configuration is shown in figure 4.30. The measurement was made with the probe 0.75cm inside the LCMS on the low field side of HSX. Note the strong angle evolution throughout the bias pulse. If the angle information were not included in the fit, the data would be much more difficult to understand.

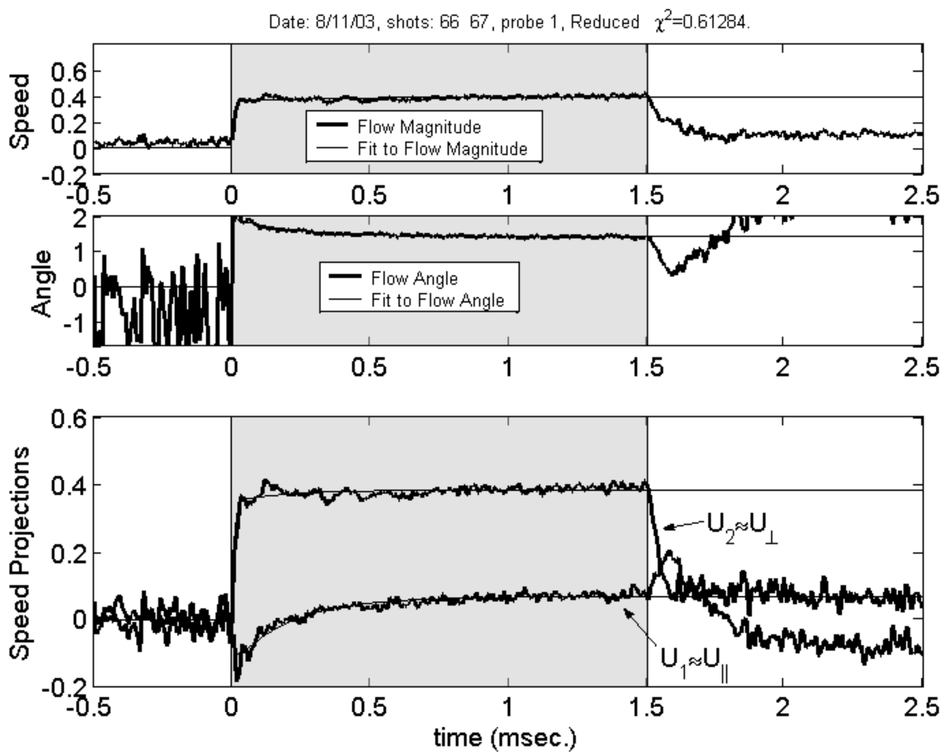

Figure 4.30: Evolution of the flow speed (top) and angle (middle) over the bias pulse, along with the flow projections (bottom) and the fits to the flow rise, for the LFS Mach probe in the Mirror configuration.

The flow decay appears to be more complicated and is not well understood. For lack of a more appropriate analysis technique, a two time scale fitting routine similar to the flow rise fit can be applied to the flow decay. This is a second fitting step and is independent of the fits of the flow rise. The decay fit functions look similar (4.3a) and (4.3b), but with the exponential forms changed:

$$\bar{U}_{1,fit}(t) = \begin{cases} C_f \,\mathbf{cos}(\alpha_f) + C_s \,\mathbf{cos}(\alpha_s) & t < t_{off} \\ \left\{ C_f \,\mathbf{exp}\left(-{(t - t_{off})}/{\tau_f}\right) \mathbf{cos}((\alpha_f)) + \right. & \\ \left. C_s \,\mathbf{exp}\left(-{(t - t_{off})}/{\tau_s}\right) \mathbf{cos}(\alpha_s) \right\} & t > t_{off} \end{cases}, \tag{4.5a}$$

$$\bar{U}_{2,fit}(t) = \begin{cases} C_f \sin(\alpha_f) + C_s \sin(\alpha_s) & t < t_{off} \\ \left\{ C_f \exp\left(-{(t - t_{off})}/{\tau_f}\right) \sin((\alpha_f)) + \right. & \\ \left. C_s \exp\left(-{(t - t_{off})}/{\tau_s}\right) \sin(\alpha_s) \right\} & t > t_{off} \end{cases}. \tag{4.5b}$$

These functions can be fit to the flow decay using the same fitting techniques as for the flow rise. An example of these decay fits is shown for the LFS probe in figure 4.31. The time window in this figure has been shortened and shifted to only display the flow decay. The top frame shows the total flow speed decay when the electrode current is broken. The fit to the flow speed is also shown, where it is calculated as $(U_{2,fit}{}^2+U_{1,fit}{}^2)^{1/2}$.

The flow angle is shown in the second frame, as well as the fit to the angle. This fit curve is calculated as $\tan^{-1}(U_{2,fit}/U_{1,fit})$. The angle data becomes very noisy as the bias induced flows decay because the DC flows have been subtracted off.

The cosine (U_1, ~|| to **B**) and sine (U_2, $\sim\perp$ to **B**) projections of the flows, as defined in equation (4.1), are shown in the bottom frame. The perpendicular flow decays in ~50μs. This allows the important observation that the fast flow decay is slower than the fast flow rise. This is very similar to the floating potential evolution, where the floating potential rise is very fast but the floating potential decay is significantly slower. The approximately parallel flow decays on a much longer time scale of ~250μs.

Considering the picture from the perspective of radial force balance, both the floating potential and the flow perpendicular to B (the flow U_2) decay in ~30-50 μs when the biased electrode current is turned off. This similarity of the time scales for fast flow decay and the floating potential decay holds across all densities and configurations (see Chapter 7), and is a standard feature of the flow relaxation. The remaining flow, which is almost all parallel, decays on a slower time scale after receiving what appears to be a small boost.

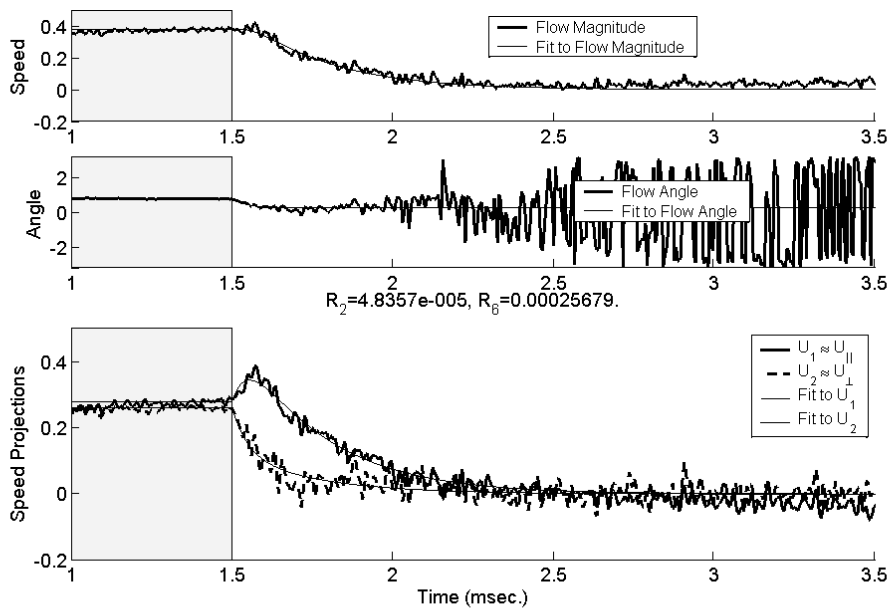

Figure 4.31: Example of the fits to the flow decay, for the LFS Mach probe. The plasmas are in the QHS configuration with a line average density of $1x10^{12}$.

The reason for this boost is not known. Under some circumstances, the behavior of the flow decay can be even more aberrant than shown in figure 4.31. The same analysis was performed on data taken with the high field side Mach probe, and is shown in figure 4.32. As in the previous example, the perpendicular flows decay very quickly. On the other hand, this case shows a substantially larger boost in parallel flow than the previous example. The two time scale fits are shown in the figure as well. These fits capture only a portion of the dynamics in the data.

The time scales extracted from these fits are approximately representative of the flow relaxation, but should be interpreted with caution. In general, this two time scale decay formalism may not be the most appropriate way to understand the flow relaxation. A different formulation of the model might allow a better extraction of the relevant physics. This is a topic for further exploration.

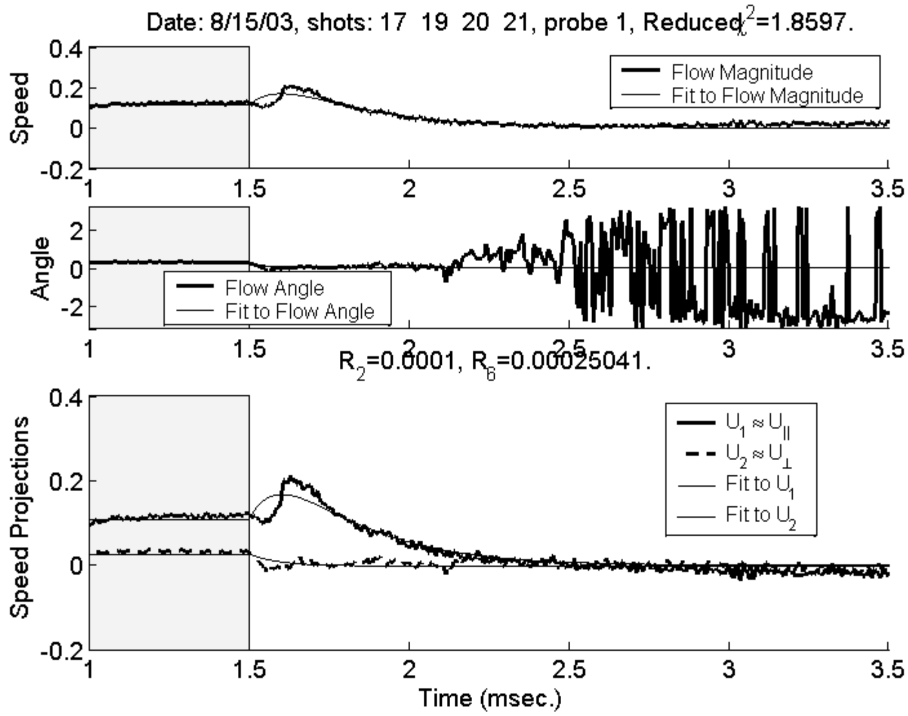

Figure 4.32: Example of the fits to the flow decay, for the HFS Mach probe. The plasmas are in the QHS configuration with a line average density of $1x10^{12}$.

It will be seen in Chapter 6 that neoclassical theory predicts two time scales for the flow and electric field decay. The floating potential decay in figure 4.24 shows only a single time scale. It might be observed that this comparison is not fair; the electric field is, after all, the spatial derivative of the floating potential. To remedy this objection, consider figure 4.33. The top frame illustrates the floating potential signals at two radial locations. The radial electric field is approximately the difference of the two floating potential measurements, and is shown in the bottom frame where the magnitude has been normalized to a maximum of one. A horizontal line illustrates that the electric field goes back to its pre-bias value on the same time scale as the floating potential decays. Hence, we infer that the longer time scale does not appear to be present in the electric field. From this point forward, the decay times of the floating potential will be used to represent the electric field dynamics.

The average flow speed evolution at the two radial locations is also shown in the lower frame of the figure. The slow time scale flows continue long after the electric field has decayed. Recall from the discussion above that these flows are observed to be mainly parallel to **B**, and so do not contribute to the electric field through radial force balance.

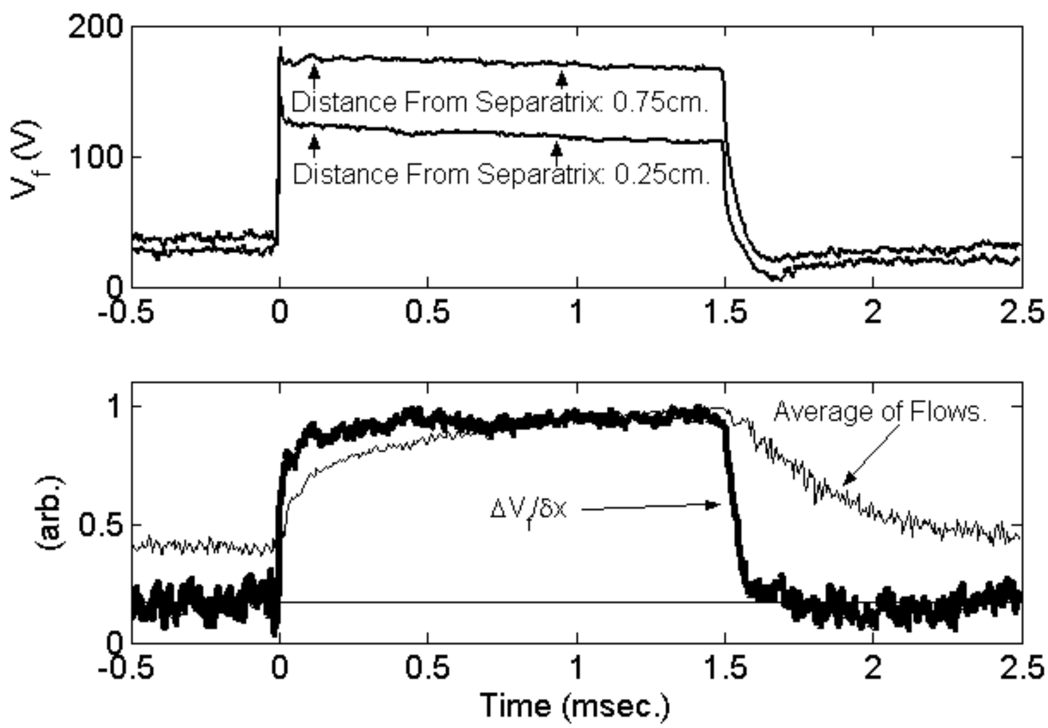

Figure 4.33: Floating potential evolution at two radial locations (top), and the inferred electric field and measured flow speed (bottom). The electric field and flow speed have been normalized for a maximum of one.

The plasma flow and floating potential evolution time scales measured by the probes on the LFS and HFS generally agree with each other quite well. The right frame of figure 4.34 illustrates the inverse time scale for slow flow rise, as measured by the two different probes. This rate is simply the inverse of the fit parameter τ_s in equation (4.3). The left frame illustrates the inverse decay time of the floating potential for the same set of discharges. The measurements with the two probes agree well with each other, both in term of numerical value and radial profile. Measurements at 2 locations on a flux surface are not sufficient to conclusively demonstrate that these time scales are flux surface quantities in the strictest sense. On the other hand, the similarity is sufficient to show that the time scales are a global quantity. Many more examples of high and low field side measurement comparisons will be provided in the context of comparisons with neoclassical theory in Chapter 7.

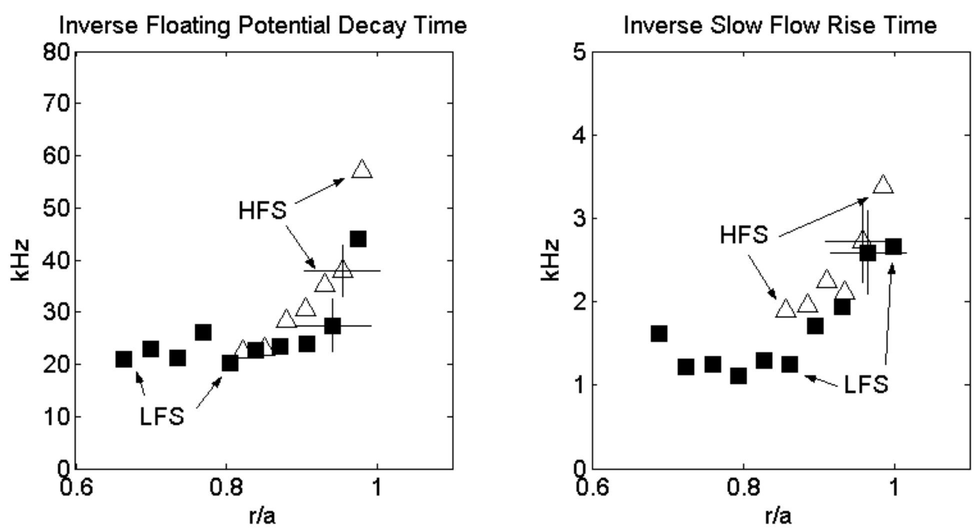

Figure 4.34: The inverse floating potential decay time (left) and inverse slow flow rise time (right), as measured on the HFS (open diamonds) and LFS (closed squares) of in the QHS configuration. Note the different scales.

The data analysis techniques presented in this section allow the extraction of flow directions and time scales from the data. These time scales and directions can be compared to predictions from modeling. This will be the subject of Chapter 7. Before that point, the modeling techniques will be discussed in detail in Chapters 5 and 6.

4.5 Comparison Between the QHS and Mirror Configurations of HSX.

The previous section illustrated data acquired by the biased electrode and Mach probe systems. Data from both the QHS and Mirror configurations were illustrated in different contexts, but not systematically compared. The comparison of these two configurations is the purpose of this section.

To illustrate some of the physics of these measurements, consider a simple one dimensional flow evolution equation,

$$mn\frac{dU}{dt} = F - \mu U, \tag{4.6}$$

$$F = \begin{cases} 0 & t < 0 \\ jB & t > 0 \end{cases}. \tag{4.7}$$

The damping linearly proportional to the flow speed mimics the form of the damping for either ion-neutral friction or linear parallel viscosity, as will be shown in Chapter 6. The differential equation can be solved to yield an expression for the flow evolution,

$$U = \begin{cases} 0 & t < 0 \\ \frac{jB}{\mu}\left(1 - \exp\left[\frac{t\mu}{nm}\right]\right) & t > 0 \end{cases}. \tag{4.8}$$

Note that as the damping coefficient μ is reduced, the flow will take longer to reach steady state, but the steady state level of flow is increased. This simple example provides guidance when looking for signs of reduced flow damping in the measurements.

The total flow speed evolution (in Mach number) for typical QHS and 10% Mirror discharges is shown in figure 4.35. The LFS Mach probe is 0.5cm inside the separatrix in each case, and the biased electrode voltage is 350V. Both discharges have a line average density of 1×10^{12} cm^{-3}. The initial flow rise is quite similar, implying that the fast time scale for flow rise is similar between the two cases. After this similar initial fast rise, the QHS case continues rising, while the Mirror case rolls over and saturates. Given that the longer rise is representative of reduced damping, this figure provides evidence of the reduced damping in the QHS configuration.

At the end of the electrode voltage pulse, the plasma flow is significantly larger in the QHS case than the Mirror case. As will be shown below, the stored energy is about 25% higher in the QHS discharges than the Mirror ones. It can thus be assumed that the electron temperature is not lower in the QHS discharges. This implies that the sound speed is probably not lower in the QHS case. Hence, the difference in flow speeds in figure 4.35 would presumably not become smaller if the sound speed was used to replace Mach numbers with actual flow velocities. Due to lack of precise knowledge of the electron temperature in these discharges, this conversion was not attempted.

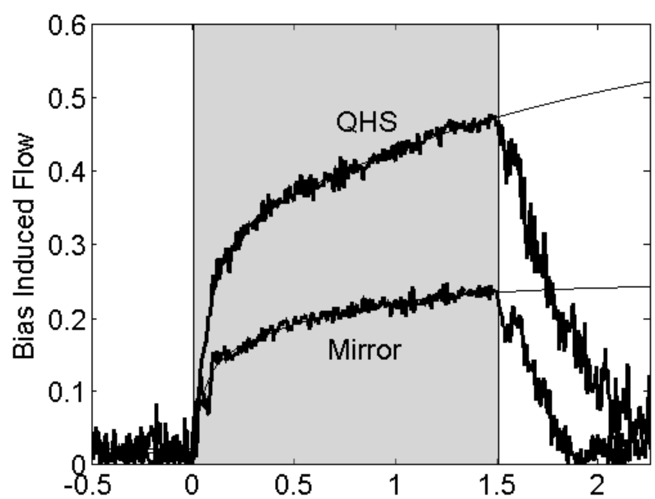

Figure 4.35: Typical Mach number evolution in QHS and 10% Mirror discharges. The duration of the electrode pulse is illustrated with the gray area.

The relaxation of the flow at the end of the voltage pulse illustrates that the decay is longer in the QHS case, again confirming the assertion that the flow damping is reduced in the quasi-symmetric case. The strange "glitch" in the total flow speed during the decay is due to the apparent rise in the parallel flow at bias turn-off, as discussed in Section 4.4.2.

The proceeding discussion can be made more concrete by examining the profiles of the different time scales for the two different configurations. Consider first the rise of the flows and potentials when the electrode voltage is applied. Both configurations exhibit an extremely fast rise in the floating potential when the voltage is applied, implying that this rise is mainly determined by the time scale over which the electrode voltage is applied. This fast flow rise time scale is extremely fast for these two configuration, and so it is difficult to make any meaningful statements based upon it. The slow rate of flow rise for the QHS and Mirror configurations is shown in figure 4.36. The slower rate of flow rise ($1/\tau_s$ in (4.3)) in these discharges illustrates the reduced damping in the QHS configuration. This data will be compared with detailed neoclassical modeling in Chapter 7.

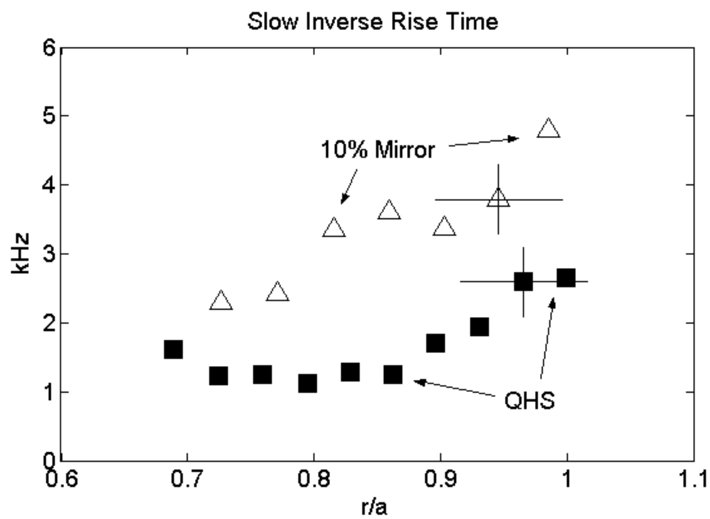

Figure 4.36: Inverse slow flow rise time, in the QHS and 10% Mirror configurations

Besides the time scales associated with the slow flow rise, the fitting routine allows the determination of how much flow is associated with the slow flow rise (the parameter C_s in (4.3)). The profiles of C_s for the same QHS and 10% Mirror discharges are shown in figure 4.37. There is a much larger increment in the slow flow for the QHS case, again confirming the reduction in damping in the QHS configuration.

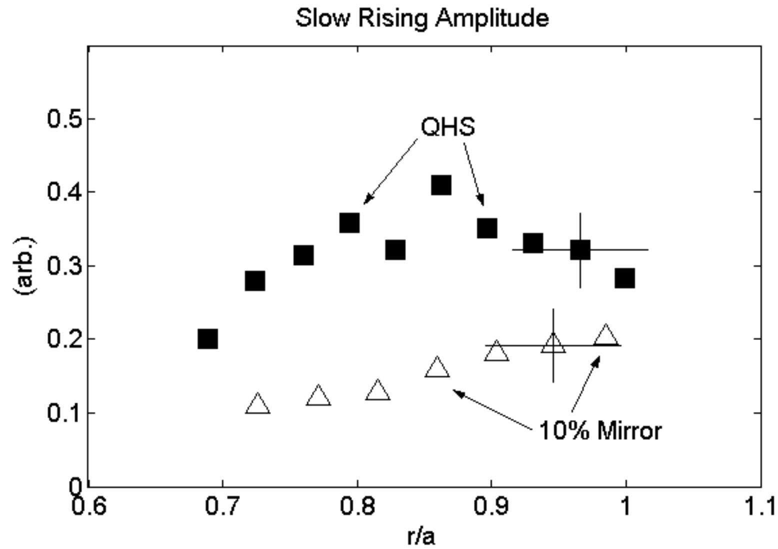

Figure 4.37: Amplitude of flow rise associated with the slow rise time scale, for QHS and 10% Mirror configurations of HSX.

Turning to the flow decay, recall that the measurements resolve two time scales for the flow to decay, as well as a time scale for the floating potential to decay. The faster time scale for the flow to decay is compared for the two configurations in figure 4.38. The figure illustrates that the time scale for the fast flow decay is approximately equal for the two configurations.

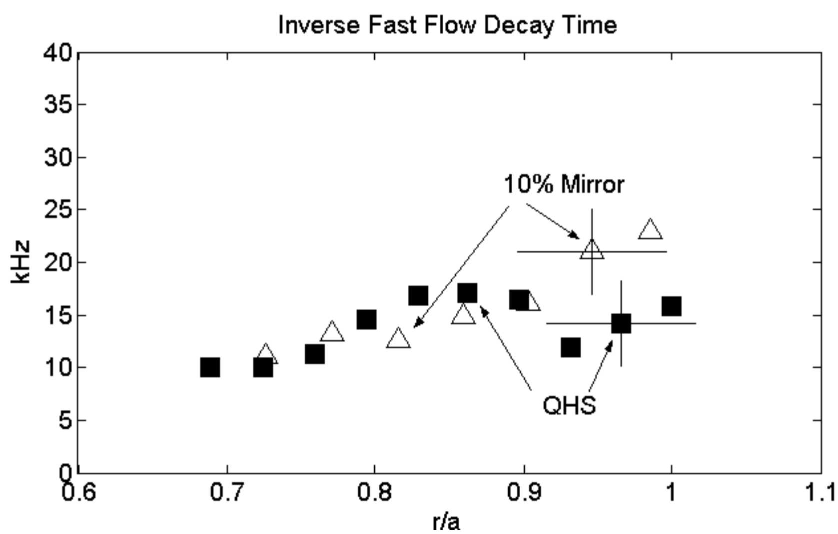

Figure 4.38: The inverse fast flow decay times for the QHS and Mirror configurations.

The inverse time for the slower flow decay ($1/\tau_s$ in (4.5)) is illustrated in figure 4.39. The Mirror configuration has a faster slow flow decay rate than the QHS, consistent with the expectations based upon neoclassical theory. It should be noted that the interpretation of this quantity is not totally clear, for the reasons discussed beneath figure 4.31. The comparisons between neoclassical modeling and measurements in Chapter 7 will demonstrate that the reduced slow flow rise rate of figure 4.36 is the strongest evidence of reduced neoclassical flow damping in the QHS configuration.

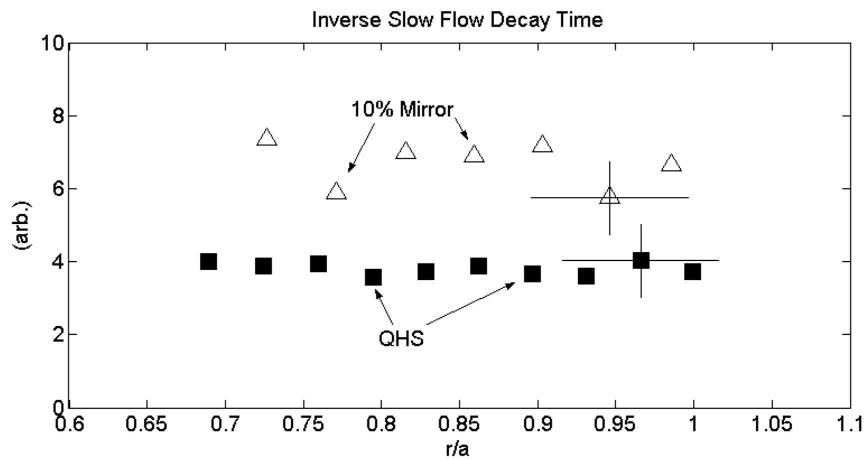

Figure 4.39: The inverse time for the slow flow to decay for the QHS and 10% Mirror configurations.

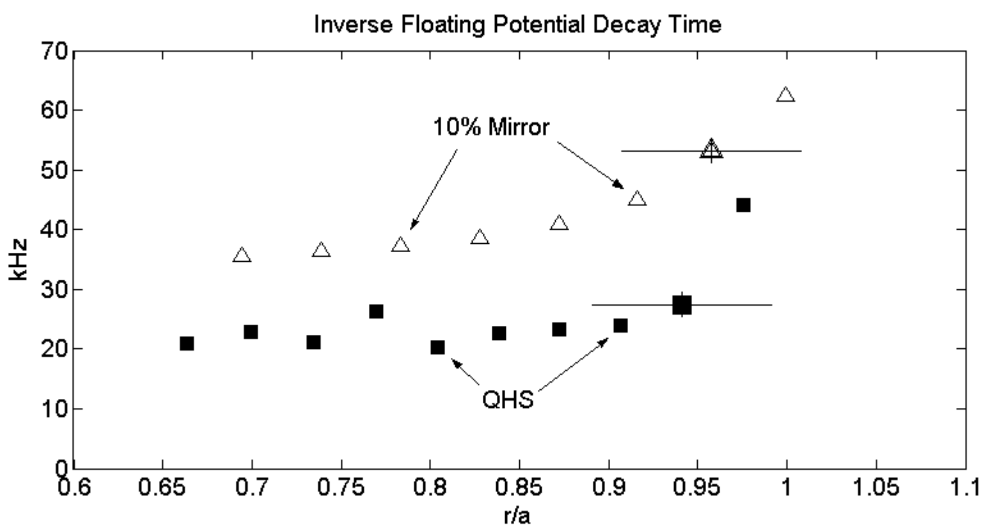

Figure 4.40: The inverse time for the floating potential to decay for the QHS and 10% Mirror configurations.

The inverse time for the floating potential to decay is shown in figure 4.40. The time scale for the floating potential to decay is similar to the time scale for the faster component of the flow to decay, although the floating potential decay appears to be somewhat faster in the Mirror configuration compared to the QHS.

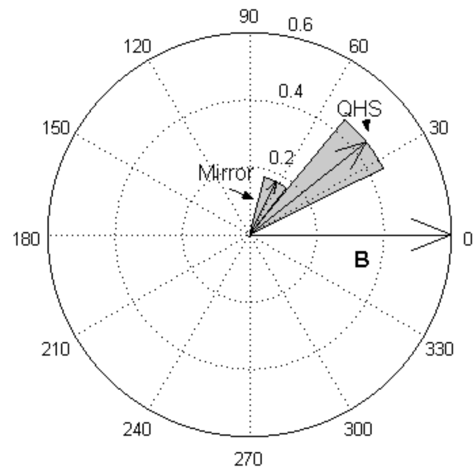

Figure 4.41: Comparison of the steady state direction of bias induced plasma flow for the QHS and Mirror configurations, as measured by the LFS Mach probe.

A comparison of the steady state flow directions in the QHS and Mirror configurations is shown in figure 4.41. The uncertainty bands indicated are indicative of the error in the calibration of the flow angle with respect to the magnetic field. The error in the relative flow directions between the QHS and Mirror configurations is smaller. There are two features to note here. The Mirror configuration flow is rotated to the counterclockwise compared to the QHS flow. This counterclockwise rotation carries the flow farther away from the direction of symmetry. Secondly, there is significantly more flow in the QHS case. This extra flow has already been noted in comparing figure 4.12 and 4.15, where a larger increment in the parallel flow was observed during bias for the QHS configuration.

Most of the data presented in this section will be discussed in more detail in Chapter 7, where it is compared to neoclassical modeling.

It is important to verify that the background plasma parameters are not significantly different for the QHS and 10% Mirror discharges under discussion here. The central chord line average density, central chord of the poloidal H_α array, stored energy, and radiated power are shown in figure 4.42, as a function of the location of the Mach probe making the flow and floating potential measurements. The biased electrode is held at a fixed location during these scans, and causes some degradation of the plasma compared to cases with no probes. These plots show that the plasma parameters are not significantly disturbed as the measuring probe is inserted. All parameters are approximately the same for the QHS and 10% Mirror cases, except the stored energy, which is lower in the 10% Mirror case by ≈20% (approximately consistent with the reduction in volume in the Mirror configuration). It can be inferred from this data that the differences in viscous damping are not due to differences in the plasma parameters in the two configurations.

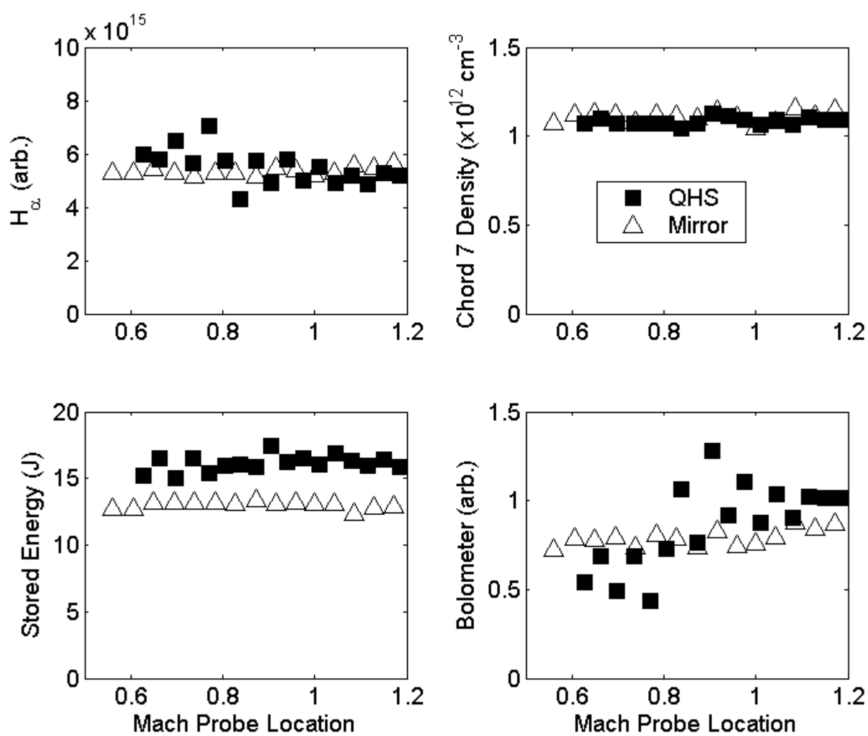

Figure 4.42: Changes in the plasma parameters as the Mach probe is inserted, for the QHS and Mirror configurations.

4.6 Turbulence Measurements in Biased Electrode Discharges.

The suite of diagnostics used to diagnose the plasma flows and potentials also provide some ability to examine turbulence in the presence of electrode bias. The floating potential measurement on the Mach probes has the ability to monitor V_f fluctuations up to a frequency of 100kHz. The Pearson current monitor in the electrode power supply is capable of monitoring fluctuations in the electrode current at frequencies up to 1MHz.

Figure 4.43 displays the QHS floating potential power spectrum both before and during the bias pulse. The discharges have a line average density of 1×10^{12} cm^{-3}. The measurement is made at approximately 0.5cm inside the last closed flux surface (LCMS). With the exception of the lowest frequencies, there is reduction in the floating potential fluctuations within the bandwidth of the measurement. A similar trend is observed when the floating potential is measured at 2.5 cm inside the LCMS (figure 4.44), except that a large coherent fluctuation is present at ~50kHz. This coherent mode appears to be unaffected by the large electric field applied by the bias. The origin of this large fluctuation is a topic of ongoing research. Note that the electrode location was fixed during the scanning of the probe making the V_f measurements.

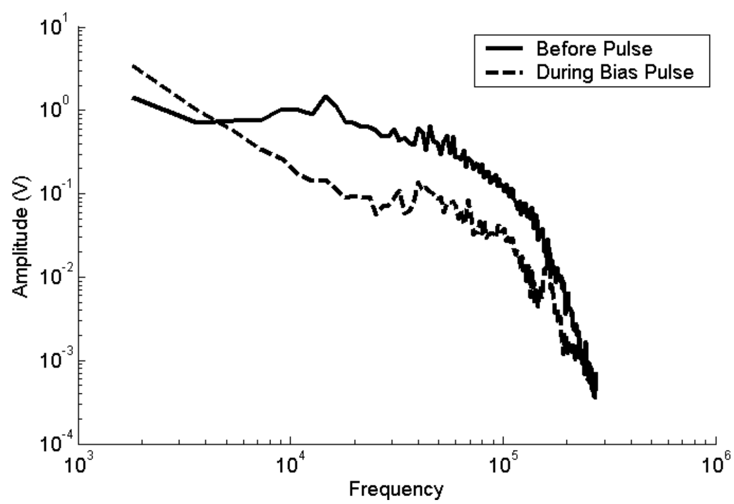

Figure 4.43: Power spectrum of V_f fluctuations, before and during the electrode voltage pulse, in the QHS configuration 0.5cm inside the LCMS

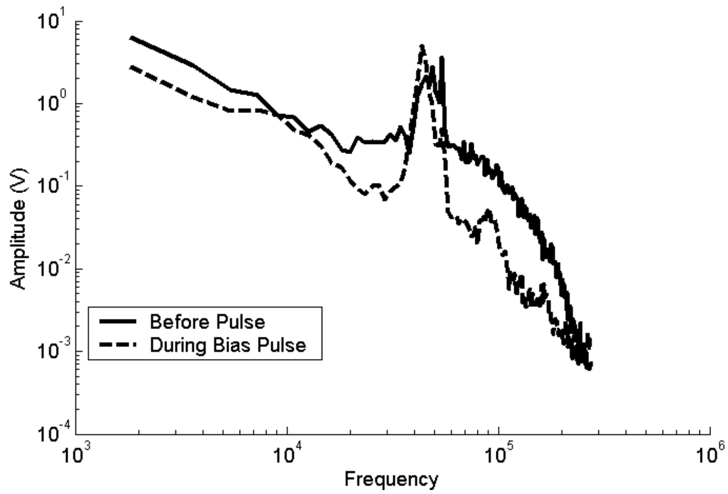

Figure 4.44: Power spectrum of V_f fluctuations, before and during the electrode voltage pulse, in the QHS configuration 2.5cm inside the LCMS

Similar measurements have been made of the fluctuations in the electrode current. The electrode current has an approximately linear relationship with the density, implying that any fluctuations in the electrode current are possibly representative of density fluctuations. Figure 4.45 shows an example of this measurement for the QHS discharge in the plots above. The 50 kHz coherent mode observed in floating potential measurements is present in this electrode current measurement as well. The fluctuation is not observed in discharges at a density of $5x10^{11}$, consistent with previous observations of this fluctuation.[16]

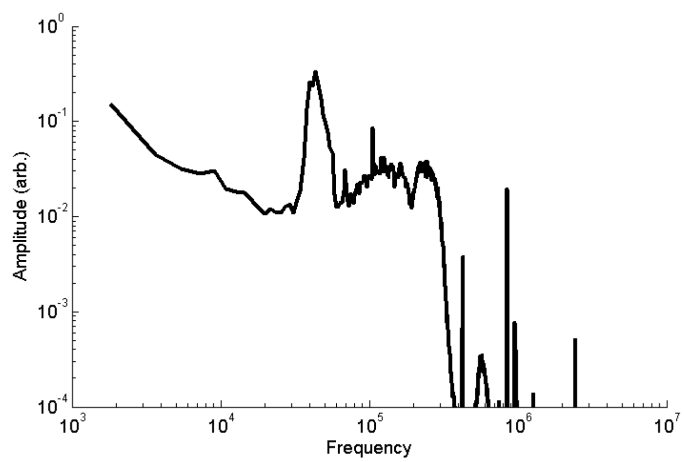

Figure 4.45: Electrode current fluctuations in the QHS configuration.

A similar measurement of the electrode current fluctuations was made for the 10% Mirror configuration of HSX, as shown in figure 4.46. These discharges, with a line average density of 1×10^{12} cm^{-3}, were very similar to the QHS discharges presented above. Note that there is a peak in the electrode current fluctuations at ≈150kHz. This is beyond the bandwidth of the microwave interferometer as it is normally operated, but similar features have been observed with high bandwidth Langmuir probes.[17] This peak continues to exist when the density is dropped to 5×10^{11} cm^{-3}, unlike the large coherent fluctuation in the QHS case.

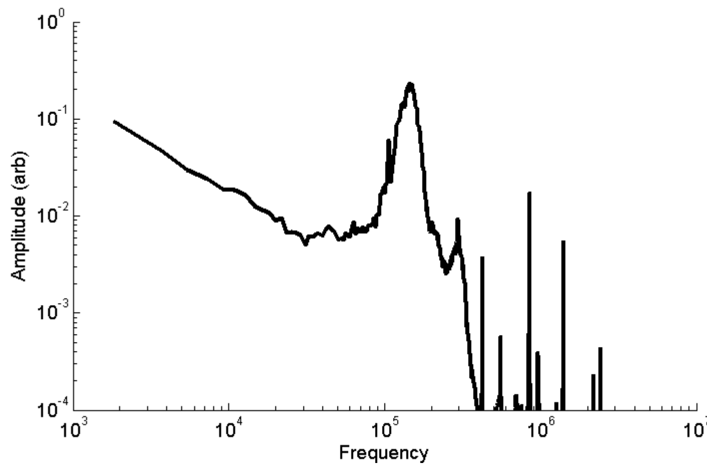

Figure 4.46: Electrode current fluctuations in the Mirror configuration.

4.7 Summary

A detailed description of HSX plasmas under electrode biasing has been provided in this chapter. The electrode current is linearly related to the voltage, and there is evidence that cross field transport limits the current collected by the electrode. No H-mode like E_r-shear layer or electrode current bifurcation[1,2] is observed.

At both bias turn-on and turn-off, the flow is measured to evolve with two time scales. On the other hand, the floating potential time evolution is very fast (~1-5 μs) when the bias is applied, but is substantially slower when the electrode current is terminated. This asymmetry between the rise and the fall will motivate the modeling discussed in Chapter 6. Measurements made on the high and low field sides of HSX illustrate similar profiles of the floating potential and evolution time scales when their radial coordinate is mapped to toroidal flux.

The QHS configuration displays features of reduced damping compared to the Mirror configuration. The flows rise more slowly at bias turn-on and decay more slowly at bias turn-off. There is substantially more flow in the QHS configuration for a given amount of electrode current.

There are indications of a reduction of particle transport with electrode bias, and evidence of a reduction in fluctuations. These observations will need to be clarified by further observations of macroscopic transport and microscopic turbulence.

[1] R.J. Taylor, M.L. Brown, B.D. Fried, J.R. Liberati, G.J. Morales, P.Pribyl, D. Darrow, and M. Ono, Phys. Rev. Lett. **63**, 2365 (1989).

[2] R.R. Weynants, G. Van Oost, G. Bertschinger, J Boedo, P. Brys, T. Delvigne, K.H. Dippel, F. Durodie, H. Euringer, K.H. Finken, D.S. Grey, J.D. Hey, D.L. Hillis, J.T.Hogan, L. Konen, R. Leners, A.M. Messiaen, A. Pospieszczyck, U. Samm, R.P. Schorn, B. Schweer, G. Telesca, R. Van Nieuwenhove, and P.E. Vandenplas, Nuclear Fusion **32**, 837 (1992).

[3] K.C. Shaing, E.C. Crume, Jr., Phys. Rev. Lett. **63**, 2369 (1989).

[4] K.C. Shaing, Phys. Rev. Lett. **76**, 4364 (1996).

[5] H. Dahi, J.N. Talmadge, and J.L. Shohet, Phys. Rev. Lett **80**, 3976 (1998).

[6] K. C. Shaing, S.P. Hirshman, and J.D. Callen, Phys. Fluids **29**, 521 (1986).

[7] Personal communication with W. Guttenfelder.

[8] G.S. Kirnev, V.P. Budaev, M.M. Dremin, E.V. Gerasimov, S.A. Grashin, L.M. Khimchenko, S.K. Krilov, et. al., Plasma Phys. Control. Fusion **45**, 337 (2003).

[9] C. Silva, H. Figueiredo, I. Nedzelsky, B. Goncalves, J.A.C. Cabral, C.A.F. Varandas, and G. Von Oost, Plasma Phys. Control. Fusion **46**, 163 (2004).

[10] L. Tramontin, L. Garzotti, V. Antoni, L. Carraro, D. Desideri, P. Innocente, E. Martines, G. Serianni, M. Spolaore, and N. Vienello, Plasma Phys. Control Fusion **44**, 195 (2002).

[11] J. Boedo, D. Gray, S. Jachmich, R. Conn, G.P. Terry, G. Tynan, G. Van Oost, R.R. Weynants, and the TEXTOR Team, Nuclear Fusion **40**, 1397 (2000).

[12] C. Deng, D.L. Brower, W.X. Ding, A.F. Almagri, D.T. Anderson, F.S.B Anderson, S.P. Gerhardt, P. Probert, and J.N. Talmadge, Rev. Sci. Instrum. 74, 1625 (2003).

[13] Personal communication with K. Zhai.

[14] Personal communication with W. Guttenfelder.

[15] I.H. Hutchinson, Plasma Phys. Control. Fusion **44**, 1953 (2002).

[16] Personal communication with C. Deng.

[17] Personal communication with W. Guttenfelder